

X-ray Observations of Optically-Selected, Radio-Quiet Quasars

I: The *ASCA* results

I.M. George^{1,2}, T.J. Turner^{1,3}, T. Yaqoob^{1,2}, H. Netzer⁴, A. Laor⁵, R.F. Mushotzky¹,
K. Nandra^{1,2}, T. Takahashi⁶

ABSTRACT

We present the result of 27 *ASCA* observations of 26 radio-quiet quasars (RQQs) from the Palomar–Green (PG) survey. The sample is not statistically complete, but reasonably representative of RQQs in the PG-survey. For many of the sources, the *ASCA* data are presented here for the first time. All the RQQs were detected except for two objects, both of which contain broad absorption lines in the optical band. We find the variability characteristics of the sources to be consistent with Seyfert 1 galaxies. A power law offers an acceptable description of the time-averaged spectra in the 2–10 keV (quasar-frame) band for all but 1 dataset. The best-fitting values of photon index vary from object to object over the range $1.5 \lesssim \Gamma_{2-10} \lesssim 3$ with a mean $\langle \Gamma_{2-10} \rangle \simeq 2$ and dispersion $\sigma(\Gamma_{2-10}) \simeq 0.25$. The distribution of Γ_{2-10} is therefore similar to that observed in other RQ AGN, and seems unrelated to X-ray luminosity. No single model adequately describes the full 0.6–10 keV (observed-frame) continuum of all the RQQs. Approximately 50% of the sources can be adequately described by a single power law or a power law with only very subtle deviations. All but one of the remaining datasets were found to have convex spectra (flattening as one moves to higher energies). The exception is PG 1411+442, in which a substantial column density ($N_{H,z} \sim 2 \times 10^{23} \text{ cm}^{-2}$) obscures $\sim 98\%$ of the continuum. We find only 5 (maybe 6) of 14 objects with $z \lesssim 0.25$ to have a

¹Laboratory for High Energy Astrophysics, Code 660, NASA/Goddard Space Flight Center, Greenbelt, MD 20771

²Universities Space Research Association

³University of Maryland, Baltimore County

⁴School of Physics and Astronomy and the Wise Observatory, The Beverly and Raymond Sackler Faculty of Exact Sciences, Tel Aviv University, Tel Aviv 69978, Israel.

⁵Physics Department, Technion, Haifa 32000, Israel

⁶Institute of Space & Astronautical Science, 3-1-1 Yoshinodai, Sagamihara, Kanagawa 229-8510, Japan

'soft excess' at energies $\lesssim 1$ keV, but find no universal shape for these spectral components. The spectrum of PG 1244+026 contains a rather narrow emission feature centered at an energy ~ 1 keV (quasar-frame). The detection rate of absorption due to ionized material in these RQQs is lower in that seen in Seyfert 1 galaxies. In part, this may be due to selection effects. However, when detected, the absorbers in the RQQs exhibit a similar range of column density and ionization parameter as Seyfert 1 galaxies. We find evidence of Fe *K*-shell emission in at least 8 RQQs. These are all low-luminosity objects, and the line parameters are consistent with other low-luminosity RQ AGN. However the construction of the mean data/model ratios for various luminosity ranges reveals a trend whereby the profile and strength of the Fe *K*-shell emission changes as a function of luminosity.

Subject headings: galaxies:active – galaxies:nuclei – galaxies:quasars – X-rays:galaxies

1. INTRODUCTION

Quasars typically emit $\sim 50\%$ of their bolometric luminosity in a spectral component generally believe to peak in the extreme UV, but encompassing the optical to soft X-ray bands (e.g. Sanders et al 1989). This emission is believed to be closely related to the accretion flow onto the putative supermassive black hole powering the copious energy output ($L_{bol} \gtrsim 10^{44}$ erg s $^{-1}$) of quasars (eg. Zel'dovich & Novikov 1964). The remainder of the bolometric luminosity, however, is emitted with almost constant power per decade of frequency over two other broad ranges of frequencies in the infrared and X-ray band (eg. Carleton et al 1987). The origin of this emission is less clear, yet it is clearly related in some way to the presence of the Active Galactic Nucleus (AGN). The spectral energy distribution (SED) of all quasars in the infrared to hard X-ray band are somewhat similar. However quasars can be divided into two classes based on the strength of the radio emission relative to that in the optical band, hence radio-quiet and radio-loud quasars (hereafter RQQs and RLQs respectively).

The X-ray band (0.1–50 keV) is thought to contain $\sim 10\text{--}30\%$ of the bolometric luminosity of most quasars. Despite two decades of study we have only a crude idea of the X-ray spectrum of the average quasar. The spectrum appears to be dominated by a

simple power law continuum at energies \gtrsim few keV (quasar frame⁷), but steepens at energies \lesssim 1 keV. The power law is thought to be related to the underlying non-thermal emission whilst the soft X-ray component to be the high energy tail of the (psuedo-thermal ?) UV bump. Both components are known to be variable and hence diagnostics of the ultimate energy release mechanism(s). Additional spectral features such as absorption by material intrinsic to the source, Fe *K*-shell emission and 'Compton-reflection' components, so useful as diagnostics in the case of Seyfert galaxies, appear to be rare in quasars (eg. Reeves et al 1997). In many respects, our knowledge of the X-ray characteristics of quasars is reminiscent of our knowledge of the lower-luminosity Seyfert 1 galaxies a decade or so ago.

Most of the studies in the X-ray band conducted to date have been performed using small or incomplete samples of sources and/or using instruments of low spectral resolution and limited bandpass. Nevertheless many studies have suggested that RLQs have flatter spectra than RQQs throughout the X-ray band. Modelling the spectra of 33 quasars in the 0.1–3.5 keV (observed frame) band obtained using the *Einstein* IPC with a power law (corrected for line-of-sight absorption), Wilkes & Elvis (1987) found mean values of the photon indices of $\langle \Gamma \rangle_{RQ} \sim 2.0$ for RQQs and $\langle \Gamma \rangle_{RL} \sim 1.5$ for RLQs. Such a trend has been confirmed from other studies of a larger number of sources with the IPC (e.g. Canizares & White 1989). Similar modelling of the spectra in the 0.1–2.4 keV (observed frame) band obtained using the *ROSAT* PSPC reveal steeper still spectral indices, but again with $\langle \Gamma \rangle_{RQ}$ greater than $\langle \Gamma \rangle_{RL}$ (eg. Laor et al 1997 and references therein). Some studies using *EXOSAT*, *Ginga* and *ASCA* have suggested RLQs also have flatter spectra than RQQs at energies \gtrsim 2 keV (e.g. Williams et al 1992; Lawson et al 1992; Reeves et al 1997). However more recent studies have disputed this, suggesting $\langle \Gamma \rangle_{RQ} \simeq \langle \Gamma \rangle_{RL} \sim 1.7$ –1.8 (Lawson & Turner 1997; Sambruna, Eracleous & Mushotzky 1999). It should be remembered that almost all the above studies note a wide dispersion in spectral indices within both RLQs and RQQs: there appears to be no generic quasar spectrum in the X-ray band.

Our original motivation of the current project was to observe a well-defined sample of PG-quasars using a single satellite (*ASCA*; Tanaka, Inoue & Holt 1994) . We planned to compare the temporal and spectral characteristics in the 0.5–10 keV (observed frame) band to other parameters such as R_L , redshift, luminosity *etc* in a sample where at least the observational selection effects were known. Unfortunately time was not awarded for the entire project.

Here we present the results of 27 *ASCA* observations of 26 RQQs. The sources were

⁷Energies are quoted in the quasar's frame throughout unless noted

selected from the PG-quasars (see §2.1), with our own observations supplemented by archival data. The resultant ‘sample’ is by no means statistically complete. However the sample is reasonably representative of the optical and radio characteristics of the RQQs in the PG-survey as a whole. Thus we may assume the *ASCA* results provide a reasonable representation of the X-ray characteristics of the RQQs in the PG-survey.

In this paper we restrict our discussion to the *ASCA* results, postponing comparison with previous X-ray observations and other multiwaveband characteristics until George et al 2000 (hereafter Paper II). In §2 we describe the observations, data reduction and preliminary analysis. In §3 we present a temporal analysis of the data, and in §4 our spectral analysis. We discuss the various results in §5 and present a summary and our conclusions in §6.

2. OBSERVATIONS, REDUCTION AND PREPARATORY ANALYSIS

2.1. The sample

The Palomar–Green (PG) survey of stellar–like objects with ultraviolet excess ($U - B < -0.44$) covers a survey area approximately a quarter of the sky (Schmidt & Green 1983; Green, Schmidt, Liebert 1986). The survey contains a statistically-complete sample of 1715 objects of which 116 are classified as either quasars or Seyfert galaxies⁸. The subdivision between quasars and Seyfert galaxies is based solely upon whether the absolute B -magnitude is greater or less than $M_B = -23.0$ mag. In the current work we make no such distinction and, for simplicity, refer to both types of object as quasars. The optical and infrared continua of 98 of the PG-quasars have been presented in Neugebauer et al (1987). The properties of the optical emission lines of 87 of the 90 PG-quasars with redshifts $z < 0.5$ have been presented in Boroson & Green (1992). The radio properties of the majority of the PG-quasars are presented in Kellermann et al (1989, 1994). From a comparison of the radio and optical flux densities ($f_{5\text{GHz}}$ and $f_{440\text{nm}}$ respectively) it was found that the majority of the sources had $R_L = f_{5\text{GHz}}/f_{440\text{nm}} \lesssim 1$, but that $\sim 20\%$ of the sources had $R_L \geq 10$. This led to the common classification into RQQs and RLQs, with the most frequently used division at $R_L = 10$.

⁸There 114 quasars and Seyfert galaxies in the complete sample listed in Schmidt & Green (1983). Boroson & Green (1992) pointed out that one of these objects (PG 0119+229) does not have broad emission lines. Later, Green et al (1986) added three objects to the complete sample (PG 1001+291, PG 1203+355 and PG 2349-014). They commented on the former two sources but not the latter.

The sample considered in this paper consists of all the radio-quiet PG-quasars for which the *ASCA* data are available to us (as of 1999 Jul 01). The data are either from our own observations, or have been extracted from the *ASCA* archive at NASA/GSFC. The sample is listed in Table 1 and is comprised of 27 observations of 25 objects. (Only four sources, PG 0003+199, PG 0050+124, PG 0921+525 and PG 1534+580 are Seyfert galaxies according to the criteria used by Schmidt & Green.) The sample is therefore approximately a quarter of the RQQs in the PG sample. Table 1 also lists the source redshift (z) from Fabian & Usher (1996, and references therein), the absolute visual magnitude⁹ (M_V) derived from Neugebauer et al (1987) or Boroson & Green (1992), the radio-loudness (R_L), and the Galactic column density of neutral material along the line-of-sight ($N_{H,0}^{gal}$) as determined from 21 cm measurements. In Fig. 1 we show the distribution of the PG sample in z , M_V and R_L along with some characteristics of the optical emission lines from Boroson & Green (1992). These are the equivalent width and FWHM of the $H\beta$ line, the equivalent width of the FeII complex between $\lambda 4434$ and $\lambda 4684$, and Peak $\lambda 5007$ – the ratio of the peak height of the [OIII] $\lambda 5007$ line to that of $H\beta$. It can be seen that the objects presented here are fairly representative of the RQQs in the whole PG sample. The *ASCA* observing log is given in Table 2, along with various related parameters and references to those datasets which have also been presented elsewhere.

2.2. Data screening

As described in the *ASCA Data Reduction Guide*, there are a number of observer-selectable choices for observations with the *ASCA* instruments. All the observations presented here have data available using so-called ‘BRIGHT-mode’ on the SIS detectors. Many of the observations also have data collected simultaneously using ‘FAINT-mode’. However, since this mode is not available for all the datasets, here we restrict our analysis to the BRIGHT-mode data. The SIS clocking mode(s) used for each observation is given in Table 2. In most cases a single clocking mode is used throughout an observation, although multiple modes are used occasionally. Two of the observations reported here (PG 1416-129 and PG 1634+706) were performed using two clocking modes. Due to small differences in the calibration, the SIS data from each mode were analysed independently. All the data from the GIS detectors were obtained using PH mode. Further details on the instrumentation on *ASCA* and its performance can be found in Makishima et al (1996, and references therein).

⁹ $H_0 = 50 \text{ km s}^{-1} \text{ Mpc}^{-1}$ and $q_0 = 0.5$ are assumed throughout.

The raw data for all but one of the observations (PG 1543+489) were converted to unscreened event files using the 'Rev2' version of the processing scripts. The event files containing data collected in all three telemetry modes were combined. These data were then screened using the `ascascreen` (v0.39) script within the `FTTOOLS` package (v4.0) such as only to include data collected when: the spacecraft was outside of the South Atlantic Anomaly; the radiation belt monitor rate was less than 500 ct s^{-1} ; magnetic cut-off rigidity was $>6 \text{ GeV/c}$; angular offset from the the nominal pointing position was $<36 \text{ arcsec}$; elevation angle above the Earth's limb was $> 5^\circ$ for GIS data, and $> 10^\circ$ for SIS data. In the case of SIS data (only), the following additional criteria were also applied: that the Bright Earth angle (elevation angle above the sun-illuminated Earth's limb) was $> 20^\circ$; that the spacecraft was at least 100 s beyond the day/night terminator. An appropriate CCD pixel threshold was chosen for each SIS dataset and 'hot' and 'flickering' pixels were removed using the standard algorithm. Only SIS 'grades' 0, 2, 3 and 4 were included in the analysis. The exposure times for the screened events files are listed in Table 2 along with other observational details.

2.3. Spatial Analysis and extraction procedure

After extracting the event files we accumulated and examined the images for each instrument. All but two of the targets (PG 0043+030 and PG 1700+518) were detected in all four instruments. For each detected source, we used `XIMAGE` (v2.30) to sum the two SIS images (in sky coordinates) and determine the source centroid. In all but one case, the X-ray centroids of the detected sources were found to be $\lesssim 1 \text{ arcmin}$ of the optical position of the host galaxy as noted in Table 1, and hence consistent with the current uncertainty in the attitude reconstruction of *ASCA* data (Gotthelf & Ishibashi 1997). Similar results were obtained using the summed GIS images. As noted in Nandra et al (1997a), an offset $\sim 1.5 \text{ arcmin}$ (to the west) was found in the case of PG 0003+199. However we are confident that the quasar is the origin of the X-ray emission as the position of the X-ray source as determined by *ROSAT* observations agrees well is that of the optical nucleus. A number of serendipitous sources were evident in the images, and are noted in the appendix.

Extraction cells were defined for the subsequent temporal and spectral analysis of the (target) PG-quasar. In the case of the *ASCA* SIS data, the source extraction cell employed was circular of radius $\sim 3.2 \text{ arcmin}$ centered on the target. From the point spread function (psf) of the XRT/SIS instrument, such a cell contains $\sim 84\%$ of the total source counts when the cell lies entirely within the active area of the SIS chip. In a number of cases, however, the pointing of the spacecraft was such that some part of the source extraction cell

falls outside the active region of the SIS chip, with a corresponding reduction in the fraction of total source counts contained. An extraction cell was defined to provide an estimate of the background for each SIS detector which consisted of the whole of the nominal CCD chip excluding a circular region of ~ 4.3 arcmin centered on the source. In the case of the GIS data, the source region was circular of radius ~ 5.2 arcmin centered on the target. From the psf of the XRT/GIS instrument the region contains $\sim 89\%$ of the total source counts. An annulus, centered on the source and covering $\sim 5.2\text{--}9.8$ arcmin was used to provide an estimate of the background for each GIS detector. For both the SIS and GIS the regions immediately surrounding the serendipitous sources were excluded from the extraction cells. All fluxes and luminosities quoted below (but *not* count rates) have been corrected for the fraction of the source photons falling outside the source extraction cells.

3. TEMPORAL ANALYSIS

Light curves of the source region were constructed for each observation using XRONOS (v4.02) and several bin sizes (t_{bin}). We combined the data from the separate instrument pairs to form SIS and GIS light curves in order to increase the signal-to-noise ratio in our analysis, but only consider bins which are fully exposed in both instruments (SIS0/SIS1 or GIS2/GIS3). Following Nandra et al (1997a), we parameterize any variability by the normalised 'excess variance', $\sigma_{rms}^2(t_{bin})$, as prescribed in Turner et al (1999a). This formulism requires there is a sufficient number of counts (n) in each bin such that Gaussian statistics are applicable, and that there is an adequate number of such bins (N). Here we adopt the requirements $n \geq 20$ and $N \geq 20$ and limit our calculation of $\sigma_{rms}^2(t_{bin})$ to those light curves in which $< 5\%$ of the original bins were excluded due to insufficient counts. The results for the 15 datasets satisfying these criteria for $t_{bin} = 256$ s are tabulated in Table 3. The quantity $\sigma_{rms}^2(t_{bin})$ is a measure of the integrated power-density spectrum of the source over frequencies f (in the quasar frame) in the range $1/t_{dur} \lesssim f/(1+z) \leq 1/N t_{bin}$, where t_{dur} is the total duration of the observation (Table 2). For all 15 datasets $1\text{--}2 \times 10^{-5} \lesssim f \lesssim 2 \times 10^{-4}$ Hz. Thus $\sigma_{rms}^2(t_{bin})$ provides a measure of the intrinsic variability characteristics over a similar range of f in all cases. From Table 3 it can be seen that statistically significant variability (at $\gtrsim 90\%$ confidence) is evident in the majority of the datasets. Inspection of the light curves for PG1404+226 reveal this source is also variable, but is too weak to satisfy our n & N criteria. Variability of lower significance may also be present in PG 1116+215 and PG 1211+143. The variable sources will be noted as appropriate within the spectral analysis presented in §4, but general discussion of the variability characteristics is postponed until §5.2.

4. SPECTRAL ANALYSIS

In the current paper we consider only the time-averaged spectra for each observation in order to maximize the signal-to-noise ratio (but bearing in mind some datasets exhibit significant variability, §3). Spectra were extracted from the source and background regions for each instrument as defined in §2.3. In the case of the SIS data, the original pulse-height assignment for each event was converted to a pulse-invariant (PI) scale using `sispi` (v1.1) and the gain-history file `sisph2pi_110397.fits`. In the case of the GIS data ‘hard particle flares’ were rejected using the so-called ‘H02’ count rate, and standard ‘rise-time’ rejection criteria. The spectral analysis was performed using the `XSPEC` (v10.00) package (Arnaud 1996), having first grouped the raw spectra such that each bin contained ≥ 20 counts permitting us to use χ^2 minimization techniques. In the case of the GIS datasets, the detector redistribution matrices released on 1995 Mar 06 were used. In the case of the SIS datasets, appropriate detector redistribution matrices were generated using `sisrmg` (v1.1). The effective area appropriate for each dataset was calculated using `ascaarf` (v2.72)¹⁰. Following common practice, for each observation we fit the spectra from all four instruments simultaneously, but allowing an independent normalization of the model for each detector to account differences in the absolute flux calibrations. All fluxes and luminosities quoted for the sources are derived (arbitrarily) using the SIS0 detector. The corresponding errors represent only the statistical uncertainties. The luminosities were calculated assuming the preferred model discussed below (with the errors derived by allowing only the normalizations of the spectral components to vary). The absolute flux calibration of the instruments on *ASCA* is believed to be uncertain by at least $\sim 5\%$.

We use a number of criteria to establish whether we consider a model to be consistent with a given dataset. During the spectral analysis we use the χ^2 -statistic (in conjunction with the number of degrees-of-freedom, *dof*) to determine the goodness-of-fit over the energy range used during the analysis. To this end, we use the probability, $P(\chi^2)$, that the statistic should be less than the observed value of χ^2 under the assumption that the model is indeed the true representation of the data. Thus $P(\chi^2) = 0.5$ corresponds to a reduced- χ^2 value of unity and values of $P(\chi^2) \sim 1$ indicate that the data are poorly represented by the model. For the purposes of this paper, we consider the model to be an adequate description of the data if $P(\chi^2) \leq 0.95$

Data from the SIS below 0.6 keV (observer-frame) were excluded from the spectral

¹⁰using the calibration files `xrt_eq_v2_0.fits` and `xrt_psf_v2_0.fits`, and including both the ‘Gaussian’ and ‘filter fudges’ to account for problems in the calibration of the instruments which have so-far defied physical explanation

analysis due to uncertainties associated with the calibration of the SIS detectors below this energy. However, although the calibration is suspect at these energies, it is generally considered that the amplitude of the error is $\lesssim 20\%$ (e.g. Orr et al 1998). Thus, following George et al (1998a), we make use of this fact by extrapolating our best-fitting models to energies < 0.6 keV and calculating the ratio of the increase in the χ^2 -statistic to the number of addition data points ($\frac{\Delta\chi_{0.6}^2}{\Delta N_{0.6}}$), and the mean data/model ratio for data points below 0.6 keV ($\overline{R_{0.6}}$). We consider models which give $\frac{\Delta\chi_{0.6}^2}{\Delta N_{0.6}} > 2$ and $\overline{R_{0.6}}$ outside the range 0.8–1.2 disagree with the data at a level unlikely to be the result of any calibration uncertainties. Such cases are noted and discussed in the text.

4.1. The X-ray Continuum

In this section we consider the form of the X-ray continuum. The goals are to obtain the simplest parametrization of the continuum consistent with the data. Thus we exclude the 5–7 keV energy band from the analysis, postponing the investigation of any Fe *K*-shell emission until §4.2.

We first compare the data to three ‘standard’ spectral models in which the underlying continuum is assumed to be a single power law. These and all other models considered in this paper include Galactic absorption *fixed* at the effective hydrogen column density ($N_{H,0}^{gal}$) derived from 21 cm measurements along the appropriate line-of-sight as given in Table 1. We use the abundances and cross-sections given in Morrison & McCammon (1983) and hence assume no variations in the abundances of heavy elements within the ISM. Our simplest model consists of only the power law. This model, hereafter referred to as **Model A**, has only one interesting parameter: Γ , the photon index of the power law. **Model B** is a single power law, absorbed by a column of neutral material at the redshift of the quasar ($N_{H,z}$) completely covering the cylinder-of-sight. This model has two interesting parameters: Γ and $N_{H,z}$. **Model C** is as for Model B, but with the absorbing material is assumed to be photoionized. The ionized-absorber models used in this paper were generated using the photoionization code ION (Netzer 1993, 1996, version ION97). The models are those used in George et al (1998a), except that here we parameterize the ionization state of the gas by a somewhat different ionization parameter defined as:

$$U_{oxygen} = \int_{538 \text{ eV}}^{10 \text{ keV}} \frac{(L_E/E)}{4\pi r^2 n_H c} dE \quad (1)$$

where L_E is the monochromatic luminosity at energy E , r the distance from the source to the absorbing material, and n_H the number density of the absorber (in all cases assumed to be 10^8 cm^{-3}). The reasoning for using this version of the ionization parameter is that the

form of the continuum at energies below the oxygen K-edge (538 eV for OI) have only a minor effect on the strength of the oxygen absorption features that are used to determine the ionization parameter and absorbing column. Model C therefore has three interesting parameters: Γ , $N_{H,z}$ and U_{oxygen} .

As will be discussed in §4.1.2, for many of the datasets, Models A–C do not provide an adequate description of the continuum over the full 0.6–10 keV (observed-frame) band. In most such cases, there appears a gradual steepening of the continuum with decreasing energy. This may not be considered surprising given the evidence for ‘soft excesses’ in previous observations of quasars. Unfortunately however, modelling (sometimes rather subtle) deviations from a powerlaw due to a convex continuum are rather problematic using *ASCA* data given the limited bandpass and the moderate spectral resolution of the instruments. Thus, it is not clear what functional form is most appropriate to model the soft X-ray emission, especially since the excesses appear to be different in different sources.

Here we have adopted two functional forms to parameterize such convex continua. The first is by introducing a second power law. In **Model D** the underlying continuum is therefore the sum of two power laws, both absorbed by a column of neutral material at the redshift of the quasar and completely covering the cylinder-of-sight. The photon indices for the ‘soft’ and ‘hard’ power laws are denoted by Γ_s and Γ_h , and the relative intensity of the components by the ratio ($R_{s/h}$) of the soft to hard power laws at 1 keV (quasar-frame). This model has four interesting parameters: Γ_s , Γ_h , $R_{s/h}$ and $N_{H,z}$. **Model E** is as for Model D except the absorbing material is photoionized¹¹, giving a fifth interesting parameter, U_{oxygen} .

The alternative functional form used to parameterize the ‘soft excesses’ is a Gaussian emission component. Thus **Model F** consists of a single power law plus a Gaussian peaking at an energy E_z , of width σ_z and total luminosity L_{line} . As will be further discussed in §4.1.2, Model F is the preferred model for a number of datasets where the Gaussian component models only small deviations from a pure power law in the 0.6–2 keV (observed-frame) band. In at least some cases this may be an artifact of remaining calibration uncertainties or an indicator of more subtle spectral complexity (see also §5.4.2).

Since the objects in our sample have a range of redshifts, the useable 0.6–10 keV *ASCA* band covers different energy bands in the quasar frame in each object (~ 2 –20 keV in the most extreme case of PG 1247-267). Thus in §4.1.1 we consider the form of the continuum in the 2–10 keV band, which enables us to make direct comparisons between the objects.

¹¹For the sake of computational expediency, the ionization state of the gas was calculated using the power law which dominates the continuum in the *ASCA* bandpass. However, in all cases the errors associated with this approximation are less than statistical uncertainties on the derived values of U_{oxygen} .

Then in §4.1.2 we consider the form of the full 0.6–10 keV (observed-frame) continuum. This obviously enables us to study the low-energy spectra of the objects with the lower redshifts and the high-energy spectra of those with higher redshifts.

We note that during the spectral analysis presented below, different portions (in energy-space) of the detectors’ response functions are used for objects of different redshift. If the sources have simple spectra across the fitted band, then this is not a concern so long as there is a section of well-constrained data from which to determine the photon index. If the sources have spectral curvature within the fitted band but are modeled using a simple power law, then the well-constrained data will occur across different parts of the curved spectrum, and could yield a false correlation between photon index and redshift, and a false distribution of photon indices. Bearing in mind these problems, in this paper we have examined the data both using a fixed rest-frame approach, and then using a fixed observed-frame approach. We base our conclusions of the sum of information from all of these fits, and do not find any evidence for instrumentally-biased results.

4.1.1. Analysis of the 2–10 keV band (quasar-frame)

In Table 4 we show the results when Model A (a single power-law with galactic absorption) is applied to the 2–10 keV band, excluding the 5–7 keV band. We find that Model A provides an adequate description of the data (i.e. $P(\chi^2) \leq 0.95$) over this restricted energy band for all but one dataset. This simple parametrization, is the least dependent on any physical model. The exception is PG 1411+442, which has an ‘inverted’ best-fitting photon index, and will be further discussed below.

In Fig. 2 we show the data/model ratios for each of the datasets when the best-fitting power law derived from this analysis is extrapolated and compared to the data in the full *ASCA* band. It can be seen that for several of the datasets the ratios are close to unity at all energies. It is important to note that these datasets are not only those with low signal to noise ratio, nor do they seem to be only the high luminosity sources. The most noticeable aspect of Fig. 2 is, however, that for the majority of the datasets the data/model ratios exhibit large, systematic deviations from unity at one or more energies. In the case of PG 1114+445 and PG 1543+489, there is a deficit of counts $\lesssim 2$ keV (observed-frame). The remainder of the sources have an excess of counts at low and/or high energies compared to the best-fitting power-law 2–10 keV continuum. It should also be noted that several of the datasets contain residuals in the 5–7 keV band indicative of Fe *K*-shell emission (see §4.2).

4.1.2. Analysis of the full 0.6–10 keV (observed-frame) Continuum

In this section we report the results from an analysis of the 0.6–10 keV (observed-frame) continuum of each dataset (again excluding the 5–7 keV band in the quasar’s frame). We have applied Models A–F to all the datasets, and for each defined the model which we consider *the simplest, acceptable description* of the data. This is defined as the acceptable model for which the inclusion of additional free parameters no longer improves the fit at $> 95\%$ confidence (using the F -statistic). The preferred model for each dataset is listed in Table 5. The derived spectra and corresponding data/model ratios are shown for a number of the datasets in Fig. 3.

The selection of our preferred model is straightforward for the majority of the datasets, and we are confident that the model provides a fair representation of the time-averaged spectrum. However, the selection of our preferred model for 3 datasets (PG 1148+549, PG 1411+442 and PG 1634+706) warrants some discussion. Models A–F do not provide a fit which satisfied all our criteria for these datasets. In the case of PG 1634+706, our preferred model is an unattenuated power law (Model A). The lack of an acceptable fit appears to be the result of excess scatter of the residuals throughout the *ASCA* bandpass, and we note $P(\chi^2)$ was only just acceptable in our 2–10 keV fits (§4.1.1 and Table 4). In the case of PG 1148+549, whilst Model A provides an acceptable description to the fitted data, it does not extrapolate in an acceptable manner below 0.6 keV ($\overline{R}_{0.6} \simeq 1.5$). This is most likely due to an additional spectral component dominating the emission below 0.6 keV. However since the *ASCA* data are unable to place useful constraints on this component, Model A is retained as our preferred model. PG 1411+442 is particularly interesting. Our preferred model is a variant on Model B in which a fraction D_f of the underlying continuum does not suffer attenuation (Model B_{pc}) whilst the remainder is absorbed by a large column density (see Fig. 3 below).

The best-fitting parameters for those datasets for which Models A–C, D–E and F are preferred are listed in Tables 6–8. In general our results are as might be expected from inspection of Fig. 2. In the case of 3 datasets (PG 1211+143, PG 1404+026, and PG 1440+356), Model F is preferred with the Gaussian component parameterizing the steepening of the spectrum at the lowest energies. A convex continuum is also apparent in 7 other datasets, but we prefer a model in which it is parameterized by a second power law (ie. Models D and E)¹². In the case of PG 0003+199 and PG 1501+106a,b, the second

¹²We acknowledge that in many cases the true spectrum is likely to be more complex than either parameterization. However, the low spectral resolution afforded by the *ASCA* detectors, the relatively low signal-to-noise ratio of the present data, and the remaining calibration uncertainties, make it difficult to

power law is a parameterization of a soft X-ray component, with $0.1 \lesssim R_{s/h} \lesssim 1$. In the case of PG 1116+215, the second power law is a parameterization of a hard X-ray component dominating the continuum at energies $\gtrsim 5$ keV ($R_{s/h} \gtrsim 10^2$), with Γ_h ‘pegging’ at the flattest value allowed in our analysis ($\Gamma_h = 0$) and $\Gamma_s - \Gamma_h \gtrsim 2.4$. In the case of PG 0804+761 and PG 1534+580, we find $1 \lesssim R_{s/h} \lesssim 10$ with both power laws of similar importance over the bulk of the *ASCA* bandpass. This is also the case for PG 1244+026 (with $R_{s/h} \sim 10$), but the spectrum also contains a rather narrow emission feature centered at an energy ~ 1 keV. Our preferred model for this source is therefore Model D plus a Gaussian emission line with $E_z = 0.96_{-0.31}^{+0.07}$ keV, $\sigma_z = 0.09_{-0.09}^{+0.16}$ keV and $L_{line} \simeq 3 \times 10^{42}$ erg s⁻¹. This feature has been noted previously in this dataset by Fiore et al (1998a) and is further discussed in §5.4.2. Inspection of Fig. 2 reveals PG 1216+069 to have very similar data/model residuals as PG 1244+026 when compared to the best-fitting power law in the 2–10 keV band (§4.1.1). However, since the parameters associated with the putative ~ 1 keV feature cannot be well-constrained using the current *ASCA* data, Model A remains our preferred model for PG 1216+069.

For the remaining 3 datasets with convex spectra (PG 0921+525, PG 0953+415, PG 1416-129), our preferred model is Model F. However in this case the Gaussian component represents only a very subtle deviation from a pure power law continuum. This may be indicative of a true, slow curvature in the underlying continuum not accounted for in Models A–E), or may be an artifact such as a residual calibration problem. However in all cases the presence of the Gaussian component does not affect any of the remaining spectral parameters more than their statistical uncertainty. Thus we retain Model F as our preferred parameterization in all 4 cases.

To summarize our results regarding the form of the continuum in the 0.6–10 keV (observed frame) band of the 25 datasets (of 24 RQQs detected):

- a single power law continuum (Model A) is the preferred model for 7 datasets/RQQs. Five of these (PG 0050+124, PG 1216+069, PG 1247+267, PG 1407+265, PG 1444+407) satisfy all our criteria and 2 other sources (PG 1148+549 and PG 1634+706) do not.
- A single power law continuum with absorption intrinsic to the quasar (Models B and C) is the preferred model for 4 datasets (PG 0844+349, PG 1114+445, PG 1322+659 and PG 1543+489), with a variant (Model B_{pc}) the preferred model in the case of PG 1411+442. The absorption features are, however, weak in the the case of

make further progress.

PG 1322+659 and PG 1543+489 (see §5.5).

- A double power law continuum (Models D and E) is preferred for 7 datasets (PG 0003+199, PG 0804+761, PG 1116+215, PG 1244+026, PG 1501+106a,b and PG 1534+580). The second power law represents a soft X-ray component in the case of 3 datasets (PG 0003+199, PG 1501+106a,b) and a hard X-ray component in the case of 1 dataset (PG 1116+215). The two power laws are equally important within the *ASCA* band for the remaining 3 datasets (see Fig. 3). PG 1244+026 also contains a ‘narrow’ emission feature at ~ 1 keV.
- Model F is the preferred model for the remaining 6 datasets/RQQs. For 3 of these (PG 1211+143, PG 1404+226, PG 1440+356) the Gaussian component parameterizes a soft X-ray component. In the remaining 3 (PG 0921+525, PG 0953-415, and PG 1416-129), the Gaussian component parameterizes only very subtle curvature in the continuum.

4.2. The Iron K-band

Using the parameterization of the continuum obtained above, we now introduce the 5–7 keV energy band into the analysis. In Table 9 we list the number of additional spectral bins (ΔN_{pts}) for each dataset included in the analysis. We also list the fractional increase in the χ^2 -statistic per additional bin ($\Delta\chi^2 / \Delta N_{pts}$) when the preferred model from §4.1.2 is applied to the data in this band. In order to better constrain any Fe *K*-shell emission we have fixed the parameters associated with the continuum at the best-fitting values derived above. A broad Gaussian emission line was added to the spectral model. We constrain the energy of the line to lie in the range $4 \leq E_z \leq 8$ keV and its width $\sigma_z \leq 2$ keV (both in the quasar’s frame). The intensity of the line is parameterized by its luminosity, $L(\text{Fe-}K)$, and its equivalent width, $EW(\text{Fe-}K)$, compared to the underlying continuum at E_z .

Constraints and upper limits on the emission line are listed in Table 9. We find the addition of the 3 additional parameters associated with the emission line significantly (F -statistic ≥ 3) improves the fit for 11 datasets. However, the data/model ratios for the two datasets with the the largest values of $EW(\text{Fe-}K)$, PG 0050+124 and PG 1444+407, reveals features more reminiscent of an unmodelled continuum component at energies $\gtrsim 5$ keV rather than a Fe *K*-shell emission (Fig. 3). Further observations are required to distinguish between these possibilities.

We postpone further discussion of the Fe *K*-shell emission until §5.6.

5. DISCUSSION

To recap, in the previous sections we have presented the results from 27 *ASCA* observations of 26 RQQs (PG 1501+106 was observed twice).

5.1. The objects not detected

Two objects (PG 0043+039 and PG 1700+518) were not detected during the *ASCA* observations. Both are known to contain broad absorption line (BAL) systems in the optical band (eg. Turnshek et al 1997) suggesting the lack of X-rays observed is most likely due to attenuation by material along the line of sight. The lack of detection of these sources by the *ROSAT* PSPC (with a bandpass up to ~ 2.5 keV in the observer’s frame) requires column densities $\gtrsim 2 \times 10^{22}$ cm $^{-2}$ (eg. Green & Mathur 1996). The lack of detection by *ASCA* (bandpass up to 10 keV) increases the required column densities to $\gg 10^{23}$ cm $^{-2}$. The results of *ASCA* observations of a number BAL quasars (including the above two sources) have been discussed recently by Gallagher et al (1999).

5.2. Time variability

In §3 we found 15 of the datasets (14 out of the 24 RQQs detected) to have a sufficient number of counts that we were able to perform an analysis of the variability characteristics. From an analysis using the normalised excess variance $\sigma_{rms}^2(t_{bin})$ with time bins of $t_{bin} = 256$ s, we found statistically significant variability (at $\gtrsim 90\%$ confidence) in 10 datasets (9 RQQs) and suspect variability in 3 others.

From an analysis of a heterogeneous sample of Seyfert 1–1.5 galaxies observed early in the *ASCA* mission, Nandra et al (1997a) found a trend whereby sources of higher luminosity exhibit a lower degree of variability. This finding confirmed the results made by previous satellites (Barr & Mushotzky 1986; Lawrence & Papadakis 1993; Green et al 1993). The anti-correlation between variability and luminosity has been further explored by Turner et al (1999a), who considered $L(2–10$ keV) versus $\sigma_{rms}(256$ s) for a larger, but still heterogeneous, collection of Seyfert 1 Galaxies from the *ASCA* archive. In Fig. 4a we show $L(2–10$ keV) versus $\sigma_{rms}(256$ s) for the RQQs presented here along with the other sources from Turner et al (excluding the 3 RL objects in the latter). As expected, the RQQs behave in a similar way to other AGN despite covering only a limited range in luminosity. All 5 RQQs with $L(2–10$ keV) $\gtrsim 10^{44}$ erg s $^{-1}$ have $\sigma_{rms}(256$ s) $\lesssim 10^{-2}$. The lack of variability in the higher luminosity datasets is not a simple case of them having a lower signal to noise ratio. For

example, $\gtrsim 4$ times as many source counts were obtained from PG 0804+761 ($L(2-10 \text{ keV}) \simeq 4 \times 10^{44} \text{ erg s}^{-1}$, $\sigma_{rms}(256 \text{ s}) \lesssim 0.3 \times 10^{-2}$) than from the second most variable source in our sample (PG 0050+124: $L(2-10 \text{ keV}) \simeq 5 \times 10^{43} \text{ erg s}^{-1}$, $\sigma_{rms}(256 \text{ s}) \simeq 4 \times 10^{-2}$).

From a study of the *ROSAT* data from 6 PG–RQQs, including PG 1440+356 and PG 1216+069, Fiore et al (1998b) found a trend whereby the objects with steeper spectra in the observed 0.1–2 keV band are more variable on timescales of 2–20 days than the objects with flatter soft X-ray spectra. Similar behavior has been suggested from the *EXOSAT* and *ROSAT* data of low-luminosity AGN (e.g. Green, McHardy & Lehto 1993; König et al 1997; Boller et al 1996). Interestingly, the RQQs presented here reveal no clear correlation between $\sigma_{rms}(256 \text{ s})$ and Γ_{2-10} , although the number of objects is admittedly small. Turner et al (1999a) also present values for Γ_{2-10} from a similar analysis as presented in §4.1.1. From Fig. 4b it can be seen that the RQQs occupy similar regions of the $\sigma_{rms}(256 \text{ s})$ – Γ_{2-10} plane as the other sources in Turner et al (1999a).

Discussion of the correlation between σ_{rms} and parameters from other wavebands, especially the width of the optical emission lines, is postponed until Paper II.

5.3. The 2–10 keV (quasar-frame) continuum

In §4.1.1 we found a single power law (Model A) provided an adequate description of the time-averaged spectra in the 2–10 keV band for all the detected RQQs except PG 1411+442. Significant variations are seen between the best-fitting values of the photon index Γ_{2-10} between the datasets, with a range $1.5 \lesssim \Gamma_{2-10} \lesssim 3$. Using the method of Maccacaro et al (1988), we find a mean $\langle \Gamma_{2-10} \rangle = 1.97_{-0.09}^{+0.08}$ and dispersion $\sigma(\Gamma_{2-10}) = 0.24_{-0.05}^{+0.08}$. The latter values are consistent with the nearby Seyfert 1 Galaxies. For example, excluding the RL objects and the RQQs presented here, the Turner et al (1999a) sample has $\langle \Gamma_{2-10} \rangle = 1.85_{-0.06}^{+0.07}$ and $\sigma(\Gamma_{2-10}) = 0.21_{-0.02}^{+0.04}$. These results are somewhat biased by the presence of multiple observations of a single object (e.g. Fairall-9, NGC 3783, NGC 5548 & Mrk 509), however its clear from Fig. 5a that the RQQs presented here occupy a similar region of the $L(2-10 \text{ keV})$ – Γ_{2-10} plane. Discussion of the results found prior to *ASCA* is postponed until the next section.

5.4. The 0.6–10 keV (observed-frame) continuum

In §4.1.2 we presented the results from an analysis of the the full 0.6–10 keV (observed-frame) continuum of each dataset. We considered a relatively small number

of spectral models, and presented that which we felt best described the time-averaged continuum of each dataset. No single model provides an adequate description of the data from all the objects. The variety of spectral forms exhibited by the RQQs is illustrated in Fig. 6. We find no obvious trends with luminosity or redshift.

The continua of 11 out of 25 datasets (11 out of the 24 RQQs detected) can be adequately described by a single power law (i.e. those datasets for which Model A, B or C was preferred). Best-fitting continua with only very subtle deviations from a power law were the preferred model for an additional 3 datasets (3 RQQs). Of the remaining 11 datasets, we found 10 to have convex continua (flattening as one moves to higher energies). In the case of 7 datasets (6 RQQs) our preferred model parameterized the continuum as the sum of two power laws (Models D and E), and for 3 datasets (3 RQQs) as a power law plus a Gaussian component at low energies (Model F). The preferred model for PG 1411+442 involves absorption only partially covering the cylinder-of-sight, and discussion is postponed to §5.5.

For 4 of the datasets for which Models D and E are preferred (PG 0804+761, PG 1116+215, PG 1244+026 and PG 1534+580), the two power laws contribute similar fractions to the observed continuum in the *ASCA* bandpass (eg. see Fig. 3). For the remaining 21 datasets a single power law dominates the observed continuum in the *ASCA* bandpass. For these we find¹³ a mean spectral index $\langle \Gamma \rangle = 1.99_{-0.08}^{+0.08}$ and dispersion $\sigma(\Gamma) = 0.20_{-0.04}^{+0.07}$. These values are consistent with most previous results from RQQs obtained using *EXOSAT* and *Ginga* in the 2–10 keV (observed-frame) band which find $\langle \Gamma \rangle \simeq 1.8$ –2.0 and $\sigma(\Gamma) \simeq 0.2$ –0.3. (e.g. Comastri et al 1992; Lawson et al 1992; Williams et al 1992; Lawson & Turner 1997). Our results are also consistent with those from *ASCA* observations in the 0.6–10 keV (observed) band of RQQs (Reeves et al 1997) and with the general distribution of Γ exhibited by Seyfert 1 Galaxies. This is illustrated in Fig. 5b in which we show $L(2$ –10 keV) versus Γ from the *ASCA* observations of the RQQs presented here, and a selection of other RQ AGN published in the literature. The RQQs presented here show a range of Γ consistent with the other objects, with no obvious relationship between Γ and $L(2$ –10 keV). Vignali et al (1999) have recently presented results from *ASCA* observations of 5 high-redshift ($z > 2$) RQQs, all of which have $L(2$ –10 keV) $\gtrsim 10^{45}$ erg s⁻¹ (none of which are reported here). They found $\langle \Gamma \rangle = 1.7 \pm 0.1$ and $\sigma(\Gamma) \sim 0.1$ and suggested higher luminosity RQQs possess flatter X-ray continua. The 3 highest luminosity RQQs in our sample ($L(2$ –10 keV) $\sim 10^{45}$ erg s⁻¹) all have $\Gamma \simeq 2$ arguing against such an hypothesis.

¹³Using Γ_h in the case of PG 0003+199, PG 1501+106a,b.

Finally we note that *Einstein* IPC observations in 0.2–3.5 keV (observed) band reveal RQQs to have $\langle \Gamma \rangle \sim 2$ (e.g. Wilkes & Elvis 1987). This is consistent with the results presented here, but somewhat flatter than *ROSAT* PSPC observations (e.g. $\langle \Gamma \rangle \sim 2.7 \pm 0.1$, Laor et al. 1997).

5.4.1. The Presence of ‘Hard-Tails’

Our preferred model in the case of PG 1116+215 consists of a ‘normal’ continuum at low energies (with $\Gamma_s \simeq 2.4$), but then flattens to $\Gamma_h = 0$ (the flattest value allowed in the analysis) at energies $\gtrsim 5$ keV. Less dramatic ‘hard-tails’ are present in our preferred model for PG 0804+761, and PG 1244+026. In addition the data/model residuals for several other sources (eg. PG 0050+124, PG 1216+069 and PG 1444+407) seem systematically greater than unity at energies $\gtrsim 5$ keV (see Fig. 3). Such features may be indicative of a real up-turn in the spectra – for example a Compton-reflection component (e.g. George & Fabian 1991) or an additional spectral component absorbed by Compton-thick material ($N_{H,z} \gtrsim 10^{24}$ cm⁻²). Alternatively such an up-turn may arise as the result of a unknown problem with the analysis/calibration of these datasets, or may be an artifact of spectral variability within the observation (variability was apparent in many of the above datasets). Future observations of these sources at energies $\gtrsim 10$ keV will be valuable.

5.4.2. Soft X-ray Excesses & 1 keV Emission Lines

For the majority of RQ AGN, extrapolation of the 1–10 keV continuum underpredicts the emission observed in the optical/UV. An up-turn in the emitted spectrum is therefore required somewhere between ~ 1 keV and the Lyman edge (13.6 eV). Many models for the so-called ‘big, blue bump’ place this up-turn in the range 0.1–1 keV, and indeed observations in this bandpass (eg. by the *Einstein* IPC and *ROSAT* PSPC) typically reveal steeper spectra than observed above 1 keV.

Our preferred model for 6 datasets (5 RQQs) contains what is often referred to as a ‘soft excess’ – a separate spectral component dominating at energies $\lesssim 1$ keV. This component is represented by a Gaussian emission feature in our preferred model for PG 1211+143, PG 1404+026, and PG 1440+356, and as a second power law for PG 0003+199 and PG 1501+106a,b. A soft excess is also implied in the case of the PG 1148+549 ($z = 0.969$) just below the *ASCA* bandpass (see §4.1.2). We repeat the remarks made in §4.1: given the limited bandpass, the moderate spectral resolution and calibration uncertainties of the

instruments on *ASCA*, we consider these functional forms to be simply *parameterizations* of the true soft X-ray emission. Other functional forms are undoubtedly also consistent with the *ASCA* data. Indeed a combination of the numerous emission lines and edges expected from ionized material both within and outside the immediate circumnuclear region can also give rise to a soft excess. Furthermore, variability is detected/suspected in the majority of these RQQs. The possibility of spectral variability within the observation therefore adds to the uncertainty on the parameters derived for the soft X-ray component.

Given the limitations of the current *ASCA* data plus the imminent launch of the *Chandra X-ray Observatory*, *XMM* and *Astro-E*, we do not dwell upon these soft X-ray components here. Nevertheless we do note that we find evidence for an additional soft component in only 5 of the 18 detected RQQs with $z \leq 0.25$ (i.e sources in which the *ASCA* bandpass allows a realistic possibility of detecting features $\lesssim 1$ keV in the quasar-frame). It is clear that such components are not universal within the *ASCA* bandpass, and even when present, vary in both spectral shape and luminosity.

The *ASCA* spectrum of PG 1244+026 contains a rather narrow emission feature centered at an energy ~ 1 keV. This feature was first discovered using the same *ASCA* data by Fiore et al (1998a). Interestingly, a similar feature has recently been noted in the *ASCA* data of the Narrow-line Seyfert 1 Galaxies Ton S180 (Turner et al 1998) and Akn 564 (Turner et al 1999b). Inspection of Fig. 2 reveals PG 1216+069 may also contain a emission feature at ~ 1 keV. Unfortunately the current *ASCA* data from this object do not allow the parameters associated with the emission to be well-constrained.

Observations with instruments of higher-resolution and bandpasses stretching to lower energies are required to reveal the true nature of the soft X-ray excesses and ~ 1 keV features.

5.5. Intrinsic absorbers

The results of the spectral analysis presented in §4.1 were obtained by fixing the Galactic column density at the value ($N_{H,0}^{gal}$) derived from HI measurements (Table 1). All our preferred models (except for Model A) contain an additional column density of absorbing material ($N_{H,z}$) which we assume to be intrinsic to the quasar. There are two sources of uncertainty which could give to a false indication of intrinsic absorption. First there may be variations in the abundances of the heavy elements within the ISM resulting in an error in the attenuation curve applied to the *ASCA* spectra (by a factor proportional to the C, N and O abundance relative to HI). Second, despite us excluding the (worse-affected)

SIS data below 0.6 keV from the analysis, there are still uncertainties in the calibration of both the SIS & GIS below 1 keV (particularly in observations towards the end of the mission). The combination of these uncertainties means that any apparently intrinsic column densities with $\lesssim \text{few} \times 10^{20} \text{ cm}^{-2}$ derived using *ASCA* data should be treated with caution. With this in mind we now discuss our results.

Our preferred model suggests intrinsic absorption in 16 datasets (15 out of the 24 RQQs detected). However, the column density of any such material, $N_{H,z}$, is inconsistent with zero at $> 90\%$ confidence for only 9 datasets (8 RQQs). Furthermore, only in the case of 5 of these 9 datasets (PG 0844+349, PG 1114+445, PG 1411+422, and both observations of PG 1501+106) are we confident that some intrinsic absorption is indeed present. For the remaining 4 datasets (PG 0804+761, PG 1116+215, PG 1322+659 and PG 1534+580) the situation is less clear. (As noted in §5.1, intrinsic absorption also offers an explanation of the non-detection of the 2 BAL quasars.)

First we discuss the 4 RQQs for which we are confident there is intrinsic absorption. Ionized material along the line-of-sight to PG 1114+445 (with $N_{H,z} \sim 2 \times 10^{22} \text{ cm}^{-2}$, $U_{\text{oxygen}} \simeq 10^{-2}$) has been discussed by George et al (1997). A column density of ionized material along the line-of-sight to PG 1501+106 ($N_{H,z} \sim 2 \times 10^{21} \text{ cm}^{-2}$, $U_{\text{oxygen}} \simeq 10^{-3}$) has been discussed by George et al (1998a). Our preferred model for PG 1411+442 contains a substantial column density ($N_{H,z} \sim 2 \times 10^{23} \text{ cm}^{-2}$) obscuring $\sim 98\%$ of the continuum, and offers an explanation of the unusual optical-to-X-ray spectrum observed for this object (see Paper II). A relatively low column density of neutral material ($N_{H,z} \lesssim 10^{21} \text{ cm}^{-2}$) is suggested by our preferred model for PG 0844+349.

Ionized material is suggested along the the line-of-sight to the remaining 4 datasets. However, the derived parameters of the ionized material in PG 1322+659 are rather extreme. The implied column density is $N_{H,z} \sim 10^{24} \text{ cm}^{-2}$, but the material is in such a high ionization state ($U_{\text{oxygen}} \sim 1$) that only relatively weak absorption features are imprinted on the spectrum (Fig. 3). However, this observation was performed towards the end of the *ASCA* mission when the calibration of the instruments is becoming increasingly uncertain. The remaining 3 objects have rather complex spectra (Fig. 3). The apparent absorption could therefore be an artifact of incorrectly modeling the emission. Confirmation is required before we can be certain that these 4 objects indeed contain absorbing material along the line-of-sight.

5.5.1. The Detection Rate of Ionized Gas

With the bandpass and spectral resolution of *ASCA*, ionized material along the line-of-sight can be detected primarily by bound-free absorption edges of OVII (739 eV) and OVIII (871 eV) imprinted in the continuum. Recent observations have shown that a large fraction of low-luminosity AGN contain such material with implied column densities in the range $10^{21} \lesssim N_{H,z} \lesssim 10^{23} \text{ cm}^{-2}$ (eg. Reynolds 1997; George et al 1998a). For example, of the 12 RQ objects with $L(2\text{--}10 \text{ keV}) < 10^{44} \text{ erg s}^{-1}$ considered by George et al (1998a), 11 were found to contain evidence for ionized material.

In addition to that presented in §4.1.2, we have performed a spectral analysis of each dataset in which the model includes both OVII and OVIII edges. In each case these edges were added to the preferred continuum (having first set $N_{H,z}$ to zero in the case of Models C and E). The results are listed in Table 10. Fig 7a shows the sum of optical depths in these edges ($\tau(\text{OVII}) + \tau(\text{OVIII})$) as a function of signal to noise ratio (S/N). Only upper limits on the optical depths are obtained for the majority of the RQQs. A similar analysis was also carried out of the objects in the George et al sample, and the results are also shown in Fig 7a. There appear to be no significant variations among the distribution of $\tau(\text{OVII}) + \tau(\text{OVIII})$ between the two samples. As expected, the data from many of the RQQs are of relatively low signal to noise ratio. In the case of PG 1114+445, the low S/N is the result of the strong absorption edges in the spectrum. Nevertheless useful constraints on the the depth of the edges can be obtained for this source. As noted above, the presence of ionized material is suggested in PG 1322+659, but with a very high ionization parameter. Indeed the material is so highly ionized that oxygen is almost fully stripped, resulting in only an upper limit on $\tau(\text{OVII}) + \tau(\text{OVIII})$.

In Fig 7b we plot $\tau(\text{OVII}) + \tau(\text{OVIII})$ versus luminosity for the RQQs and George et al sample. Only objects with a $S/N > 25$ (hence excluding the RQQs with S/N less than that for any of the sources in the George et al sample). are shown, plus PG 1114+445. In the luminosity range $10^{43} < L(2\text{--}10 \text{ keV}) \leq 10^{44} \text{ erg s}^{-1}$ we find evidence for significant OVII and OVIII edges in all 8 RQ AGN from the George et al sample, yet in only 2 of the 7 RQQs (4 of 10 RQQs if no threshold is imposed on S/N). A study of a larger, well-defined sample is required to determine whether this is a selection effect. At luminosities $L(2\text{--}10 \text{ keV}) > 10^{44} \text{ erg s}^{-1}$ we find 2 out of the 3 RQQs with $S/N > 25$ contain evidence of significant OVII and OVIII edges (3 out of 9 RQQs if no threshold is imposed on S/N). The George et al sample only contains 3 objects with such luminosities, one of which has significant OVII and OVIII edges. A study of a larger number of objects covering a wider range of luminosity is required to determine whether the detection rate of ionized material changes as a function of luminosity.

Finally in Fig 8 we show the location of the ionized material in the $N_{H,z}-U_{oxygen}$ plane for the RQQs and the other objects in the George et al sample. We find no significant difference between the two samples.

5.5.2. An Absorption Line in PG 1404+226 ?

Using the same *ASCA* data reported here, Leighly et al (1997) found PG 1404+226 to contain an absorption feature at ~ 1 keV (observed-frame) which they interpreted as due to oxygen in a highly relativistic outflow. Ulrich et al (1999) also report the results of the same dataset and find an absorption feature at ~ 1 keV, but prefer alternative interpretations.

With our preferred model we find no requirement for such features in this object. For example adding 2 narrow absorption lines to our model at the energies found by Leighly et al we obtain a reduction in χ^2 of only 2.2. This lack of a significant detection is in part due to the different parameterizations of the soft X-ray emission in this source used here and by Leighly et al. We assume a Gaussian component whilst Leighly et al use a multiple black-body spectrum (Ulrich et al assume single-temperature black-body spectrum). These functional forms all intersect the underlying power law close to 1 keV. Since the significance of the absorption features is dependent on the form of the soft X-ray spectrum, future observations with higher spectral resolution are required to verify their presence. Nevertheless, we do find upper limits on the equivalent widths of the putative lines of $EW(1.12 \text{ keV}) \lesssim 64 \text{ eV}$ and $EW(1.24 \text{ keV}) \lesssim 15 \text{ eV}$ (at 90% confidence) consistent with the results of Leighly et al.

5.6. The Fe- $K\alpha$ line

In §4.2 we found the inclusion of a broad, Gaussian emission line significantly improved our preferred model in the Fe K -shell regime for 11 datasets (10 out of the 24 RQQs detected). However some doubt was however cast on the reality of such a feature in PG 0050+124 and PG 1444+407. Unfortunately the parameters associated with the Gaussian are very poorly constrained in most of the individual datasets, preventing detailed searches for trends with other parameters. For the 9 datasets (8 RQQs) in which we are confident of the presence of Fe K -shell emission, we find a mean equivalent width $\langle EW(\text{Fe-}K) \rangle = 220_{-60}^{+70} \text{ eV}$ and mean line energy of $\langle E_z \rangle = 6.34_{-0.12}^{+0.13} \text{ keV}$. The dispersions of both distributions are ill-determined with upper limits of $\sigma(EW(\text{Fe-}K)) \lesssim 450 \text{ eV}$ and $\sigma(E_z) < 0.21 \text{ keV}$ at 90% confidence. These results are consistent with

those of Nandra et al (1997b) for their sample of Seyfert 1 Galaxies when they employed a Gaussian emission component to parameterize any Fe K -shell emission ($\langle EW(\text{Fe-}K) \rangle = 160 \pm 30$ eV, $\langle E_z \rangle = 6.34 \pm 0.04$ keV and $\sigma(EW(\text{Fe-}K)) \lesssim 90$ eV, $\sigma(E_z) < 0.09$ keV at 90% confidence).

All 9 RQQs in which we detect Fe K -shell emission and all the objects reported in Nandra et al (1997b) have $L(2\text{--}10 \text{ keV}) < \text{few} \times 10^{44} \text{ erg s}^{-1}$. Based on a heterogeneous sample of Seyfert 1 Galaxies and (RL & RQ) quasars observed during the first 2 years of the *ASCA* mission, Nandra et al (1997c) have presented evidence of a change in the profile and strength of the Fe K -shell emission as a function of luminosity. They found $EW(\text{Fe-}K)$ decreased with increasing $L(2\text{--}10 \text{ keV})$ confirming such a suggestion based on *Ginga* observations (Iwasawa & Taniguchi 1993). Nandra et al also found evidence that the blue-wing of the line profile was stronger than the red-wing in sources with $L(2\text{--}10 \text{ keV}) \sim 10^{44}\text{--}10^{46} \text{ erg s}^{-1}$, contrary to case in the lower luminosity sources. This can be interpreted as the result of Fe becoming more ionized in higher luminosity sources.

In Fig. 9a we compare $EW(\text{Fe-}K)$ versus $L(2\text{--}10 \text{ keV})$ for the RQQs presented here to a selection of other RQ AGN (Nandra et al 1997b; Vaughan et al 1999; Reeves et al 1997; Vignali et al 1999). In Fig. 9b we show E_z versus $L(2\text{--}10 \text{ keV})$ for those sources with detected Fe K -shell emission. No significant trends in the Fe K -shell emission as a function of $L(2\text{--}10 \text{ keV})$ are obvious from either plot. However in Fig. 10 we show the mean data/model ratios for all the RQQs presented here for different ranges of $L(2\text{--}10 \text{ keV})$. The plots were created using the SIS data (only) and our preferred model for the continuum in each dataset (§4.1.2). The resultant data/model ratios were then corrected to the quasar frame, and co-added and rebinned for clarity. The mean profile for the RQQs with $L(2\text{--}10 \text{ keV}) < 10^{44} \text{ erg s}^{-1}$ is very similar in its intensity and profile to that often seen in Seyfert 1 Galaxies (eg cf Fig 1 in Nandra et al 1997c), with a narrow peak at 6.4 keV (corresponding to FeI–XII) and a broader base. The presence of a red-wing at energies below 6.4 keV is of particular interest as this is commonly interpreted as the result of relativistic effects close to the putative supermassive black hole (eg. Tanaka et al 1995). Unfortunately the low signal to noise ratios prevents any meaningful constraints being placed on such ‘diskline’ models using the individual datasets not already studied by Nandra et al (1997b).

We find no significant change in the intensity or profile for the RQQs with $L(2\text{--}10 \text{ keV}) = 10^{44\text{--}44.5} \text{ erg s}^{-1}$ although it should be noted that there are only 3 objects in this sub-set. In §4.2 we found the inclusion of Fe K -shell emission did not significantly improve the fits to any of the RQQs with $L(2\text{--}10 \text{ keV}) > 10^{44.5} \text{ erg s}^{-1}$. However Fig. 10 reveals evidence for such emission in the 6 datasets with $L(2\text{--}10 \text{ keV}) = 10^{44.5\text{--}45} \text{ erg s}^{-1}$. Furthermore the peak in the mean profile is consistent with being at a higher energy. However we note that

the limits on the intensity of the line in one of the datasets in this sub-set, PG 0953+415 ($EW(\text{Fe-K}) < 60$ eV), is incompatible with that of the mean profile and should serve as a reminder that there will undoubtedly be object-to-object variations within any luminosity class. Finally the mean data/model ratio for the 4 datasets with $L(2\text{--}10 \text{ keV}) > 10^{45} \text{ erg s}^{-1}$ is consistent with unity at all energies. Thus the results for the RQQs presented here confirm the results of Iwasawa & Taniguchi (1993) and Nandra et al (1997c).

6. SUMMARY & CONCLUSIONS

We have presented the results from 25 *ASCA* observations of 24 RQQs from the PG sample. Our main findings are summarized as follows:

1. All but two objects (PG 0043+039 & PG 1700+518) were detected.
2. We found 15 of the datasets to have a sufficient number of counts that we were able to perform an analysis of the variability characteristics. Significant variability was found in 10 of these datasets (9 RQQs) at $\gtrsim 90\%$ confidence. Visual inspection of the light curves suggests 3 additional sources also exhibit variability, but the signal to noise ratios are insufficient to allow statistical testing and/or it being quantified. The variability characteristics of these RQQs were consistent with the trend found by Nandra et al (1997a) and Turner et al (1999) whereby sources of higher luminosity sources exhibit a lower degree of variability.
3. We found a power law offers an acceptable description of the time-averaged spectra in the 2–10 keV band for all but 1 of the detected sources (PG 1411+442). The best-fitting values of photon index vary from object to object over the range $1.5 \lesssim \Gamma_{2-10} \lesssim 3$. The distribution of Γ_{2-10} is similar to that observed in other RQ AGN, and seems unrelated to X-ray luminosity. For the RQQs presented here we find a mean $\langle \Gamma_{2-10} \rangle \simeq 2$ but with a significant dispersion $\sigma(\Gamma_{2-10}) \simeq 0.25$.
4. No single model adequately describes the full 0.6–10 keV (observed-frame) continuum of all the RQQs. We found the continua of 14 RQQs could be adequately described by a single power law (11 RQQs) or a power law with only very subtle deviations (3 RQQs). The preferred model for PG 1411+442 has $\sim 2\%$ of the continuum escaping the nucleus directly, but the remainder attenuated by a substantial column density of material. All the remaining objects were found to have convex spectra (flattening as one moves to higher energies).

5. We find evidence for a flattening of the continuum at energies $\gtrsim 5$ keV in 5 RQQs. Although there are physical explanations for such a spectral component, the *ASCA* data are unable to exclude other possibilities.
6. Six of the 10 datasets (5 out of 9 RQQs) with convex spectra contain a 'soft excess' at energies $\lesssim 1$ keV. This component was *parameterized* by a Gaussian emission feature in the case of 3 datasets (3 RQQs) and as a second power law for the remainder. A sixth RQQ, PG 1148+549, probably contains such a component just below the *ASCA* bandpass. There is no universal soft X-ray spectrum for RQQs. For instance, out of 14 objects with $z \lesssim 0.25$ (such that there is a possibility of detecting an upturn in the spectrum $\lesssim 1$ keV), only 5 contain a 'soft excess'.
7. The spectrum of PG 1244+026 contains a rather narrow emission feature centered at an energy ~ 1 keV. A similar feature is present in the spectra of at least two Narrow-line Seyfert 1 Galaxies.
8. We find evidence for absorption by ionized material in 6 RQQs. However we are only confident of its presence in 2 objects: PG 1114+445 (with $N_{H,z} \sim 2 \times 10^{22}$ cm $^{-2}$) and PG 1501+106 ($N_{H,z} \sim 2 \times 10^{21}$ cm $^{-2}$). Three of the remaining RQQs have rather complex spectra raising the possibility that the presence of ionized absorber is an artifact of incorrectly modelling the soft X-ray spectrum. The derived parameters of the ionized material in PG 1322+659 rather extreme, but require confirmation. There are indications that the detection-rate of ionized material is lower in RQQs compared to Seyfert galaxies. However it is premature to make any definitive statements.
9. Our preferred model for PG 1411+442, in which a substantial column density ($N_{H,z} \sim 2 \times 10^{23}$ cm $^{-2}$) obscures ~ 98 % of the continuum, and offers an explanation of the unusual optical-to-X-ray spectrum observed for this object (Paper II).
10. We detect significant Fe *K*-shell emission in 10 RQQs (although there is some doubt in the case of 2 of these), all of which have $L(2-10 \text{ keV}) < \text{few} \times 10^{44}$ erg s $^{-1}$. We find the strength and energy of the emission to be consistent with that seen in other RQ AGN. However construction of the mean data/model ratios using all 25 datasets, but for different ranges of $L(2-10 \text{ keV})$, reveals a trend whereby the profile and strength of the Fe *K*-shell emission changes as a function of luminosity, consistent with previous suggestions (Iwasawa & Taniguchi 1993; Nandra et al 1997c).

We thank Fabrizio Fiore for useful discussions and an anonymous referee for suggested improvements to the paper. We acknowledge the financial support of the Universities

Space Research Association (IMG, KN, TY), LTSA grant NAG 5-7385 (TJT), and the Israel Science Foundation (HN). This research has made use of the Simbad database, operated by the Centre de Données astronomiques de Strasbourg (CDS); the *VizieR* Service for Astronomical Catalogues, developed by CDS and ESA/ESRIN; and of data obtained through the HEASARC on-line service, provided by NASA/GSFC.

A. APPENDIX: SERENDIPITOUS SOURCES WITHIN THE FIELDS OF VIEW

Besides the target, a number of additional sources were evident with the fields of view (fov) of the *ASCA* detectors. The useable portion of the GIS detectors is circular with a radius of ~ 20 arcmin. The celestial coordinates and GIS2 count rates of the serendipitous sources detected are listed in Table 11, along with a tentative identification and any references discussing X-ray observations. The FWHM of the point spread function (psf) of the GIS detectors is ~ 3 arcmin at 1 keV, and the uncertainties on the positions listed in Table 11 are ~ 20 arcsec. Each SIS detector consists of a 2×2 array of CCDs, with each CCD having a $\sim 11.2 \times 11.2$ arcmin fov. The psf of the SIS detectors is dominated by that of the focussing opticals, consisting of a relatively sharp core (FWHM ~ 0.8 arcmin), but broad, azimuthally-dependent wings (extending out to several arcmin). All 4 CCDs on each SIS were active only for one of the observations reported here (Table 2). The subsequent reduction in the SIS fov for the majority of the observations resulted in an accurate position and count rate for only one of the serendipitous sources: that in the PG 1247+267 field, with an SIS0 count rate of $3.2 \pm 0.3 \times 10^{-3}$ ct s $^{-1}$ in the 0.6–10 keV band (observer’s frame).

REFERENCES

- Arnaud, K.A., 1996, in ASP Conf. Proc. 101, *Astronomical Data Analysis Software and Systems V*, eds. G. Jacoby, J.Barnes (San Fransico: ASP), p17
- Barr, P., Mushotzky, R.F., 1986, *Nature*, 320, 421
- Boller, T., Brandt, W.N., Fink, H.H., 1996, *A&A*, 305, 53
- Boroson, T.A., Green, R.F., 1992, *ApJS*, 80, 109
- Brinkmann, W., Wang, T., Matsuoka, M., Yuan, W. 1999, *A&A*, 345, 43
- Canizares, C.R., White, J.L., 1989, *ApJ*, 339, 27
- Carleton, N.P., Elvis, M., Fabbiano, G., Willner, S.P., Lawrence, A., Ward, M., 1987, *ApJ*, 318, 595
- Comastri, A., Setti, G., Zamorani, G., Elvis, M., Wilkes, B.J., McDowell, J.C., Giommi, P., 1992, *ApJ*, 384, 62
- Elvis, M., Lockman, F.J., Wilkes, B.J., 1989, *AJ*, 97, 777
- Fabian, D., Usher, P.D., 1996, *AJ*, 111, 645
- Fiore, F., et al., 1998a, *MNRAS*, 298, 103
- Fiore, F., Laor, A., Elvis, M., Nicastro, F., Giallongo, E., 1998b, *ApJ*, 503, 607
- Gallagher, S.C., Brandt, W.N., Sambruna, R.M., Mathur, S., Yamasaki, N., 1999, *ApJ*, 519, 549
- George, I.M., Fabian, A.C., 1991, *MNRAS*, 249, 352
- George, I.M., Nandra, K., Turner, T.J., Celotti, A., 1994, *ApJ*, 436, L59
- George, I.M., Nandra, K., Laor, A., Turner, T.J., Netzer, H., Mushotzky, R.F., 1997, *ApJ*, 491, 508
- George, I.M., Turner, T.J., Netzer, H., Nandra, K., Mushotzky, R.F., Yaqoob, T., 1998a, *ApJS*, 114, 73
- George, I.M., Turner, T.J., Mushotzky, R.F., Nandra, K., Netzer, H., 1998b, *ApJ*, 503, 174
- George, I.M., Mushotzky, R.F., Turner, T.J., Yaqoob, T., Ptak, A., Nandra, K., Netzer, H., 1998c, *ApJ*, 509, 146
- George, I.M., Netzer, H., Laor, A., Turner, T.J., Yaqoob, T., Mushotzky, R.F., Nandra, K., Takahashi, T., 1999, in preparation (Paper II)
- Gotthelf, E.V., Ishibashi, K., 1997, in *X-Ray Imaging and Spectroscopy of Cosmic Hot Plasmas*, eds. F.Makino, K.Misuda (Tokyo: Universal Academy Press), p631

- Green, A.R., McHardy, I.M., Lehto, H.J., 1993, MNRAS, 265, 664
- Green, P.J., Mathur, S., 1996, ApJ, 462, 637
- Green, R.F., Schmidt, M., Liebert, J., 1986, ApJS, 61, 305
- Iwasawa, K., Taniguchi, Y., 1993, ApJ, 370, L61
- Kellermann, K.I., Sramek, R., Schmidt, M., Shaffer, D.B., Green, R., 1989, AJ, 98, 1195
- Kellermann, K.I., Sramek, R., Schmidt, M., Green, R.F., Shaffer, D.B., 1994, AJ, 108, 1163
- König, M., Staubert, R., Wilms, J., 1997, A&A, 326, L25
- Laor, A., Fiore, F., Elvis, M., Wilkes, B.J., McDowell, J.C., 1997, ApJ, 477, 93
- Lawrence, A., Papadakis, I., 1993, ApJ, 414, L85
- Lawson, A.J., Turner, M.J.L., 1997, MNRAS, 288, 920
- Lawson, A.J., Turner, M.J.L., Williams, O.R., Stewart, G.C., Saxton, R.D., 1992, MNRAS, 259, 743
- Leighly, K., 1999, ApJ, in press
- Leighly, K.M., Mushotzky, R.F., Nandra, K., Forster, K., 1997, ApJ, 489, L25
- Lockman, F.J., Savarge, B.D., 1995, ApJS, 97, 1
- Maccacaro, T., et al., 1988, ApJ, 326, 680
- Makishima, K., et al., 1996, PASJ, 48, 171
- Morrison, R., McCammon, D., 1983, ApJ, 270, 119
- Murphy, E.M., Lockman, F.J., Laor, A., Elvis, M., 1996, ApJS, 105, 369
- Nandra, K., George, I.M., Turner, T.J., Fukazawa, Y. 1996, ApJ, 464, 165
- Nandra, K., George, I.M., Mushotzky, R.F., Turner, T.J., Yaqoob, T., 1997a, ApJ, 476, 70
- Nandra, K., George, I.M., Mushotzky, R.F., Turner, T.J., Yaqoob, T., 1997b, ApJ, 477, 602
- Nandra, K., George, I.M., Mushotzky, R.F., Turner, T.J., Yaqoob, T., 1997c, ApJ, 488, L91
- Netzer, H., 1993, ApJ, 411, 594
- Netzer, H., 1996, ApJ, 473, 781
- Neugebauer, G., Green, R.F., Matthews, K., Schmidt, M., Soifer, B.T., Bennett, J., 1987, ApJS, 63, 615
- Orr, A., Yaqoob, T., Parmar, A.N., Piro, L., White, N.E., Grandi, P., 1998, A&A, 337, 685
- Reeves, J.N., Turner, M.J.L., Ohashi, T., Kii, T., 1997, MNRAS, 292, 468

- Reynolds, C.S., 1997, MNRAS, 286, 513
- Sambruna, R.M., Eracleous, M., Mushotzky, R.F., 1999, ApJ, in press
- Sanders, D.B., Phinney, E.S., Neugebauer, G., Soifer, B.T., Matthews, K., 1989, ApJ, 347, 29
- Schmidt, M., Green, R.F., 1983, ApJ, 269
- Stocke et al (1991) ApJS, 76, 813
- Tanaka, Y., Inoue, H., Holt, S.S., 1994, PASJ, 46, L37
- Tanaka, Y., et al., 1995, Nature, 375, 659
- Turner, T.J., George, I.M., Kallman, T., Yaqoob, T., Zycki, P.T., 1996, ApJ, 472, 571.
- Turner, T.J., George, I.M., Nandra, K., 1998, ApJ, 508, 648
- Turner, T.J., Nandra, K., George, I.M., Turcan, D., 1999a, ApJ, in press.
- Turner, T.J., George, I.M., Netzer, H., 1999b, ApJ, in press
- Turnshek, D.A., Monier, E.M., Sirola, C.J., Espey, B.R. 1997, ApJ, 476, 40
- Ulrich, M.-H., Comastri, A., Komossa, S., Crane, P., 1999, A&A, in press
- Vaughan, S., Reeves, J., Warwick, R.S., Edelson, R., 1999, MNRAS, in press
- Vignali, C., Comastri, A., Cappi, M., Palumbo, G.G.C., Matsuoka, M., Kubo, H., 1999, ApJ, 516, 582
- Williams, O.R., et al., 1992, ApJ, 389, 157
- Wilkes, B.J., Elvis, M., 1987, ApJ, 323, 243
- Yaqoob, T., Serlemitsos, P.J., Mushotzky, R.F., Madejski, G.M., Turner, T.J., Kunieda, H., 1994, PASJ, 46, 173
- Zel'dovich, Ya.B., Noovikov, I.D., 1964, Sov. Phys. Dokl., 158, 811

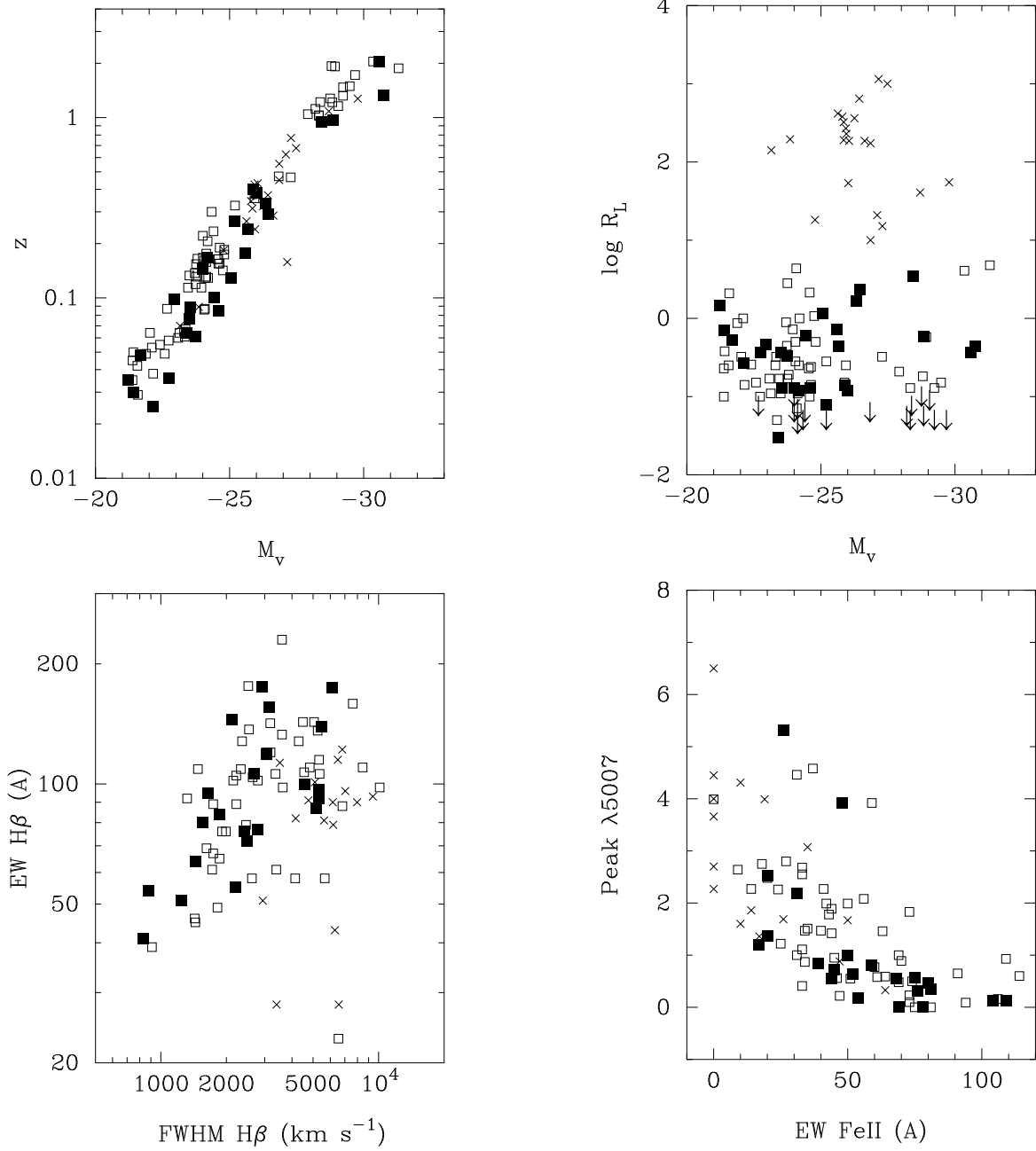


Fig. 1.— The properties of the RQQs presented here (bold) compared to the entire PG-sample. The data are taken from the references cited in the text. Other RQQs in the sample are denoted by open squares, and RLQs by crosses. The sources presented here are fairly representative of RQQs in the entire sample.

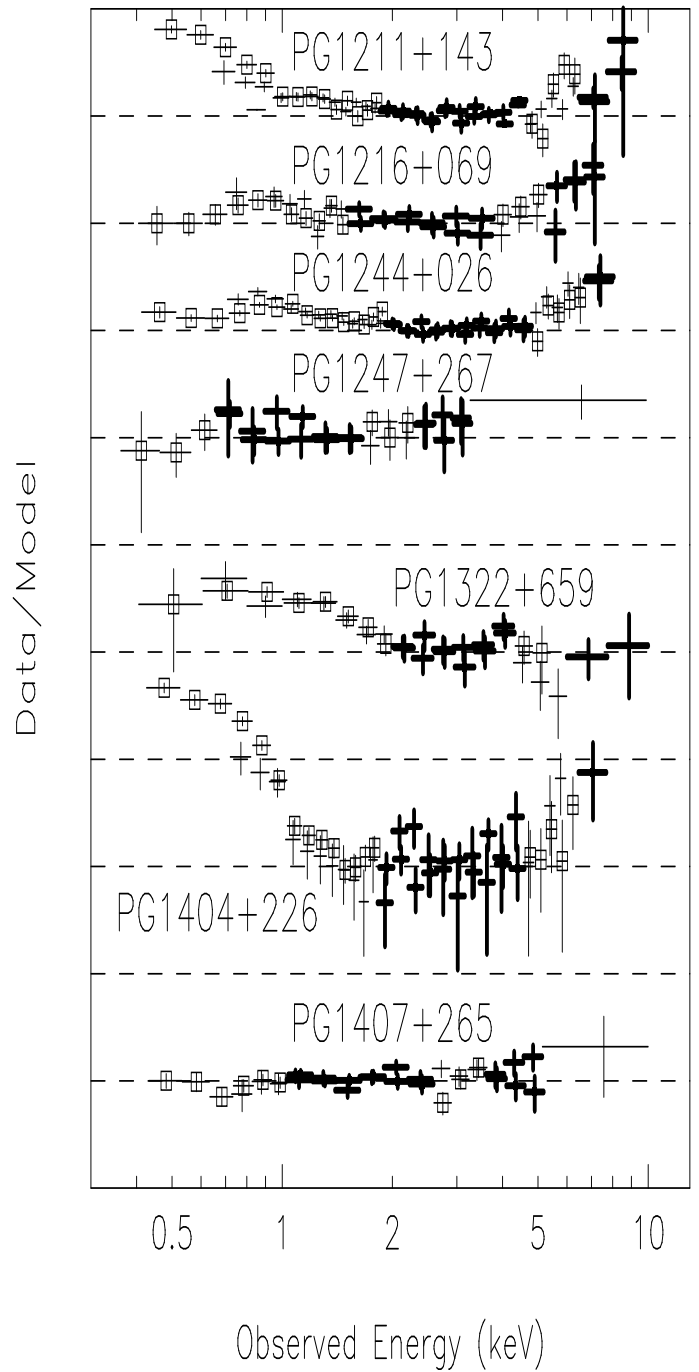
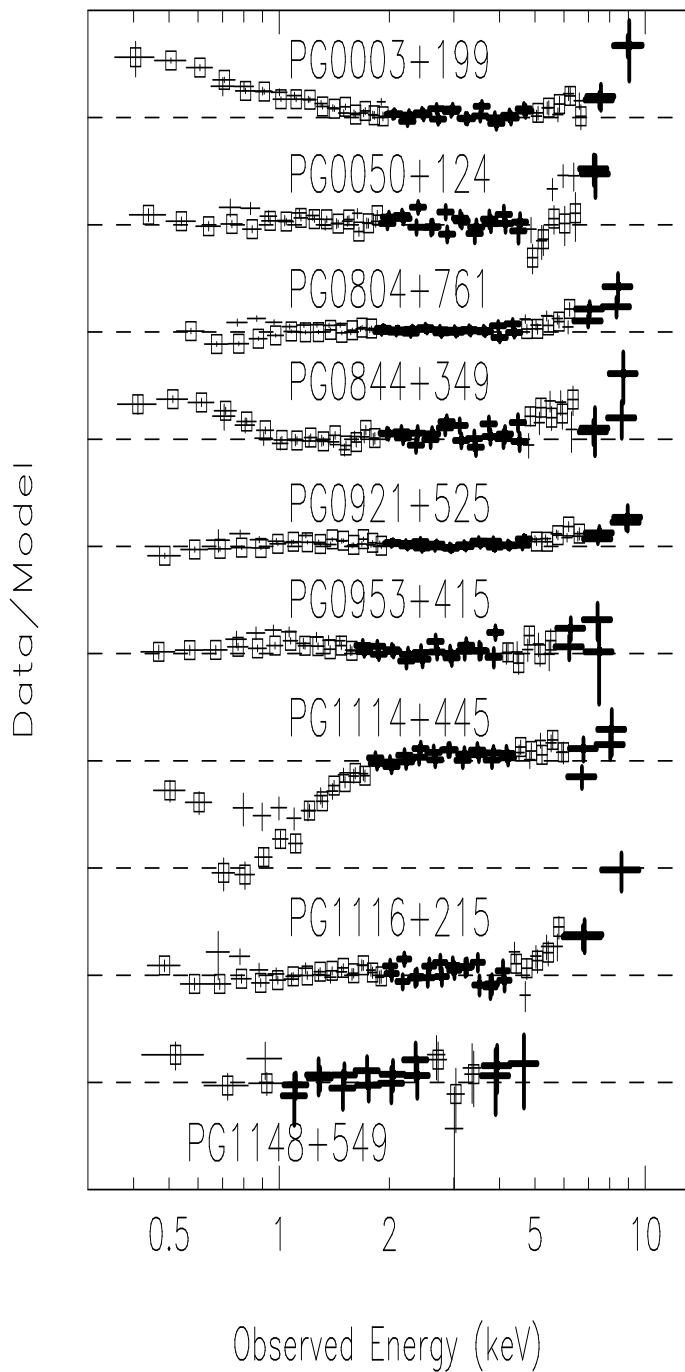


Fig. 2.— Data/model ratios obtained when the best-fitting power law to the 2–10 keV continuum (in quasar’s frame; data shown in bold) is extrapolated through the rest of the *ASCA* data. The data are the averages of each instrument pair (with the SIS data denoted by the boxes), and have been rebinned in energy-space for clarity. The y-axis is logarithmic, and the dashed lines separated by a factor of four. The model provides an adequate description of the data fitted in all cases except PG 1411+442.

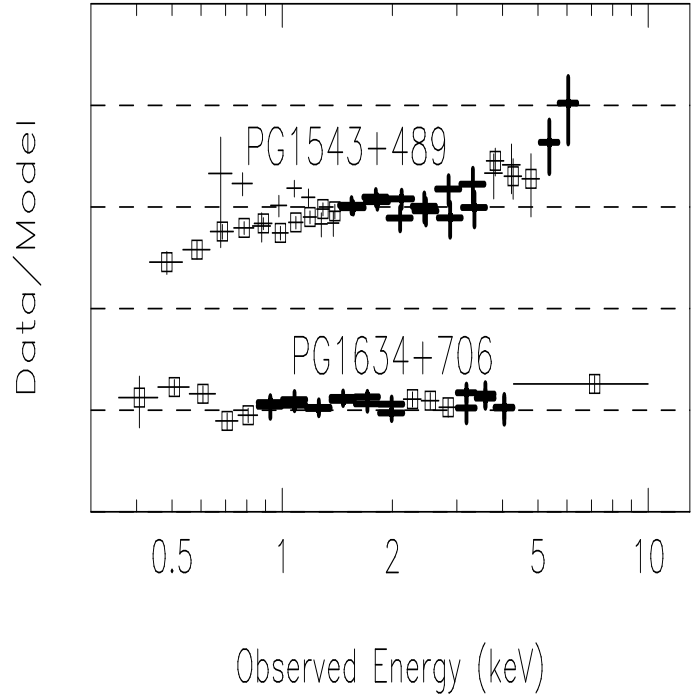
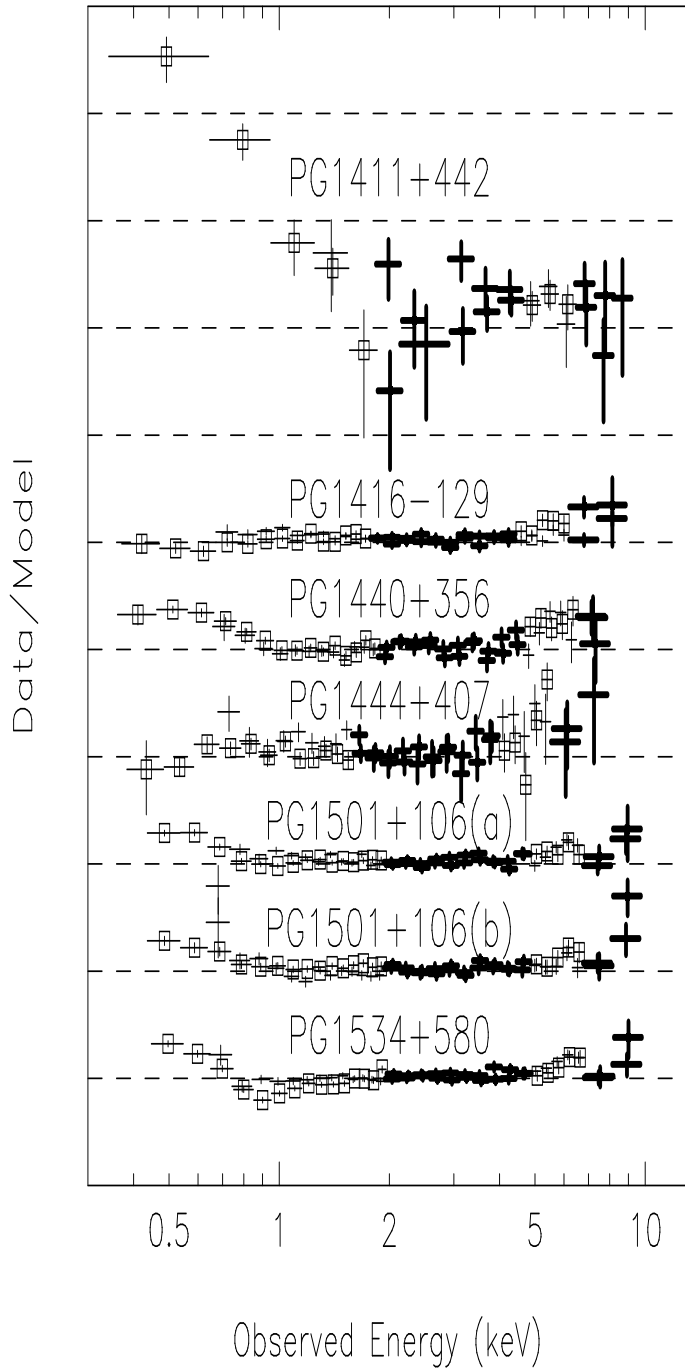


Fig. 2.— *continued*

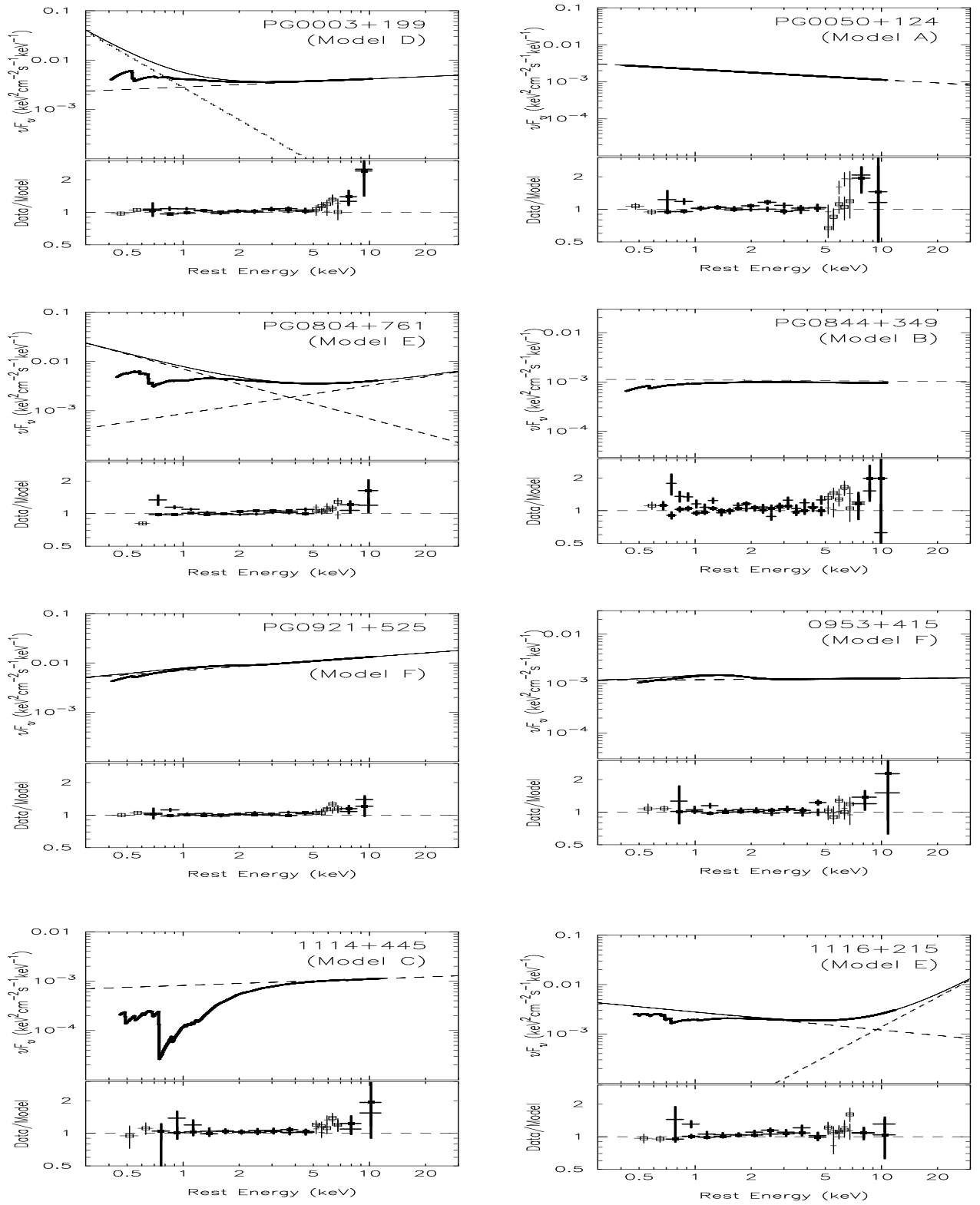


Fig. 3.— The best-fitting continua (excluding the Fe *K*-shell band) for each dataset (see §4.1.2). In each case the *bold line* in the upper panel shows the best-fitting model over the *ASCA* bandpass after correcting for Galactic absorption, the *dashed line* shows the underlying power law component(s), and (for models D–F only) the *thin solid line* shows total underlying spectrum. The lower panel shows the mean data/model ratios as for Fig. 2, except here the 0.6–10 keV (observed frame) band is used in the fits, and the range of the logarithmic y-axis is 0.5–3.0.

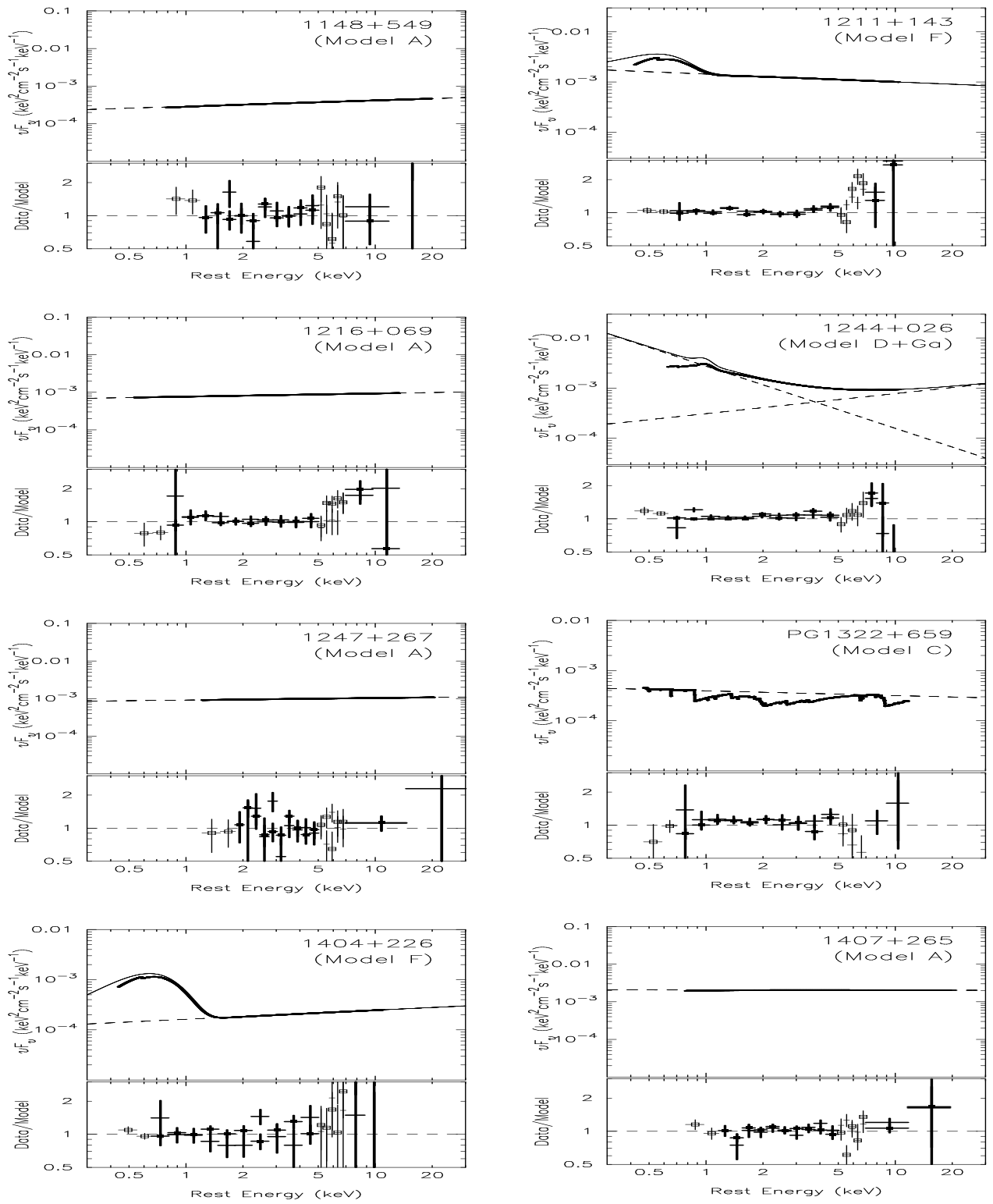


Fig. 3.— *continued*

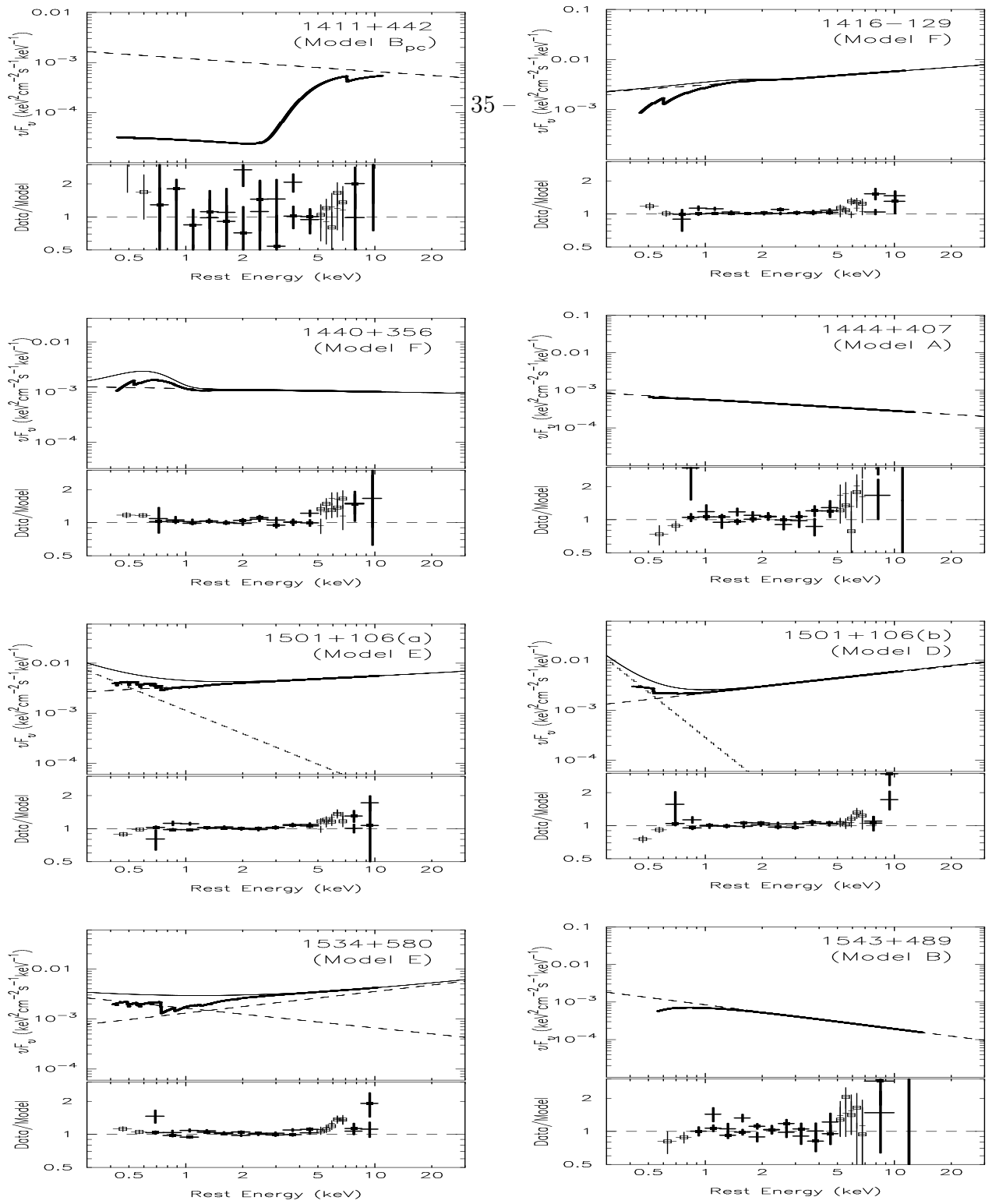


Fig. 3.— *continued*

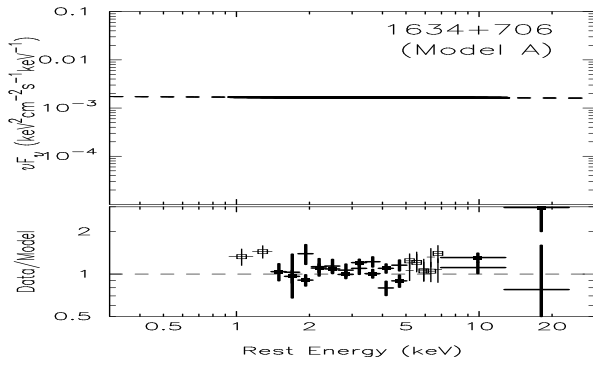


Fig. 3.— *continued*

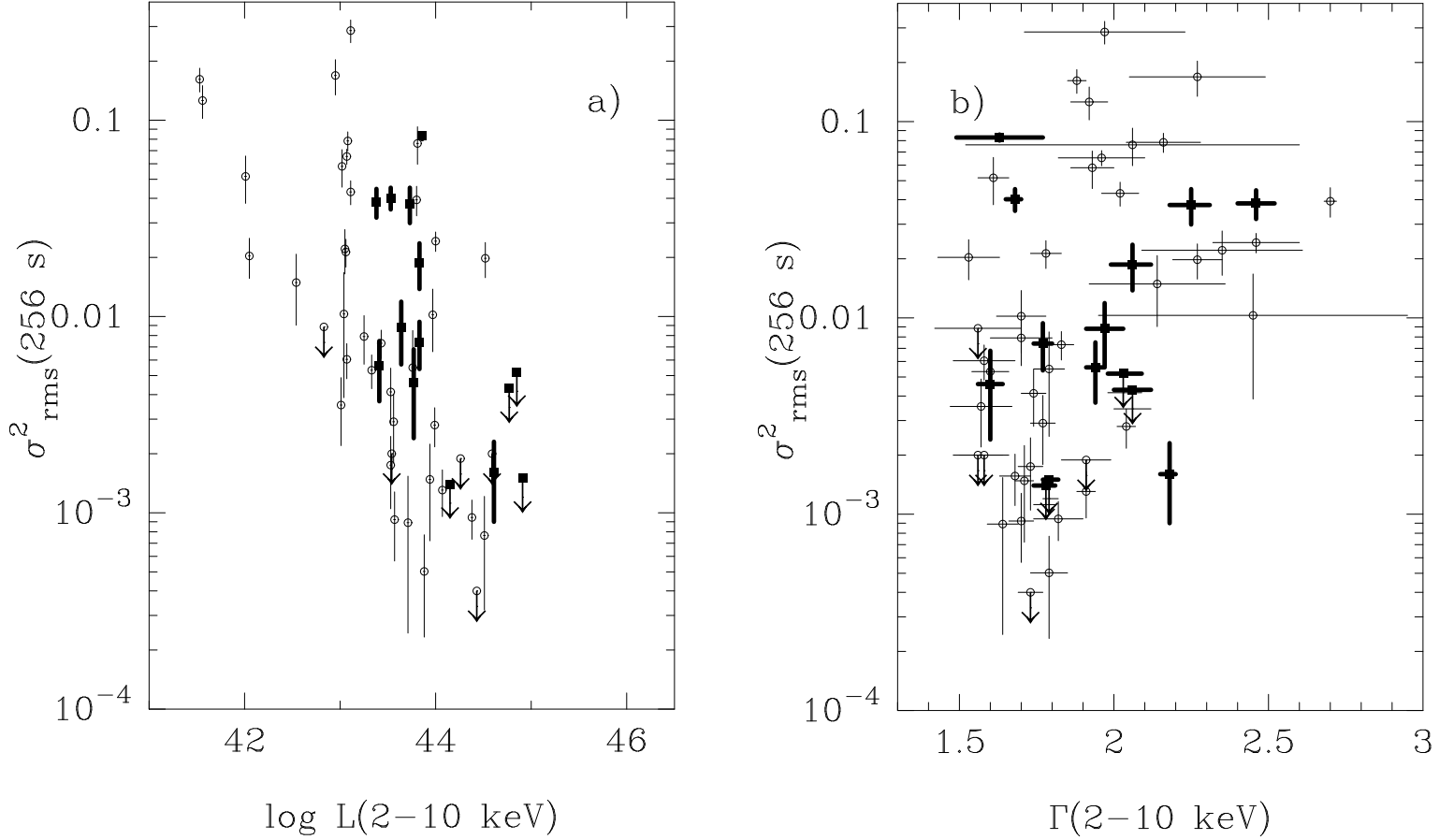


Fig. 4.— a) The excess variance, $\sigma_{rms}(256 \text{ s})$, against luminosity in the 2–10 keV band, $L(2-10 \text{ keV})$ in units of erg s^{-1} . The bold squares indicate the RQQs presented here, and the circles show other RQ AGN adapted from Turner et al (1999a). The RQQs behave in a similar way to other AGN despite covering only a limited range in luminosity. b) $\sigma_{rms}(256 \text{ s})$ against the photon index in the 2–10 keV band, Γ_{2-10} , for the same set of objects. We find no significant correlation, but do note a trend whereby most of the sources exhibiting significant variability have either 'soft excesses' or steeper than average continua.

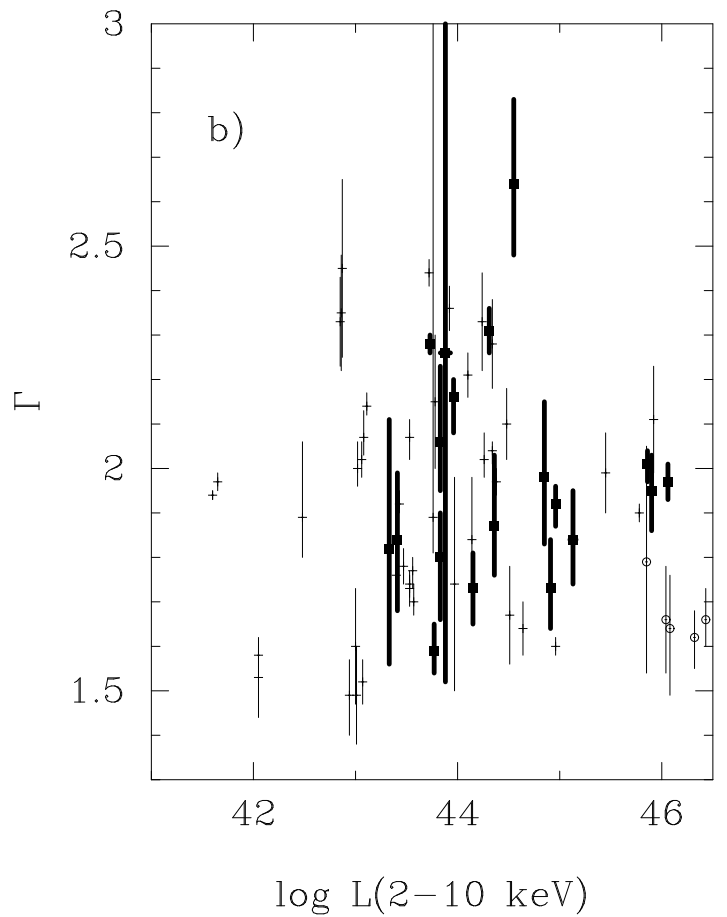
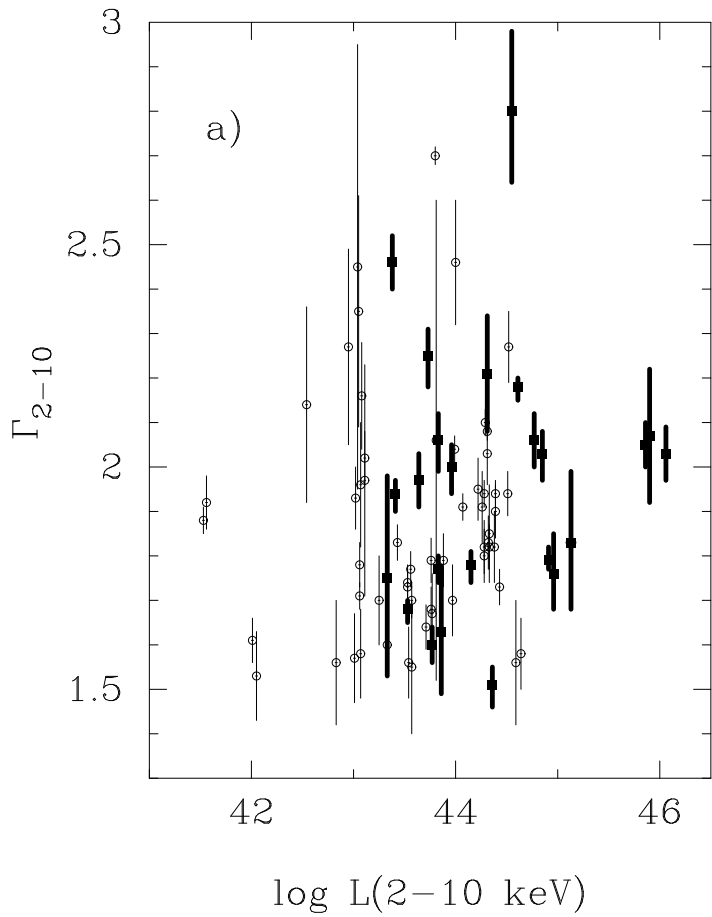


Fig. 5.— a) Luminosity in the 2–10 keV band, $L(2-10 \text{ keV})$ in units of erg s^{-1} , versus Γ_{2-10} for the RQQs presented here (bold), and the other RQ objects from Turner et al (1999a). b) $L(2-10 \text{ keV})$ versus Γ from the analysis of the 0.6–10 keV (observed frame) continuum. The crosses are the RQQs from Reeves et al (1997) along with Seyfert 1 Galaxies published in George et al (1998a,b,c) and Vaughan et al (1999). The circles are the high- z RQQs from Vignali, et al (1999).

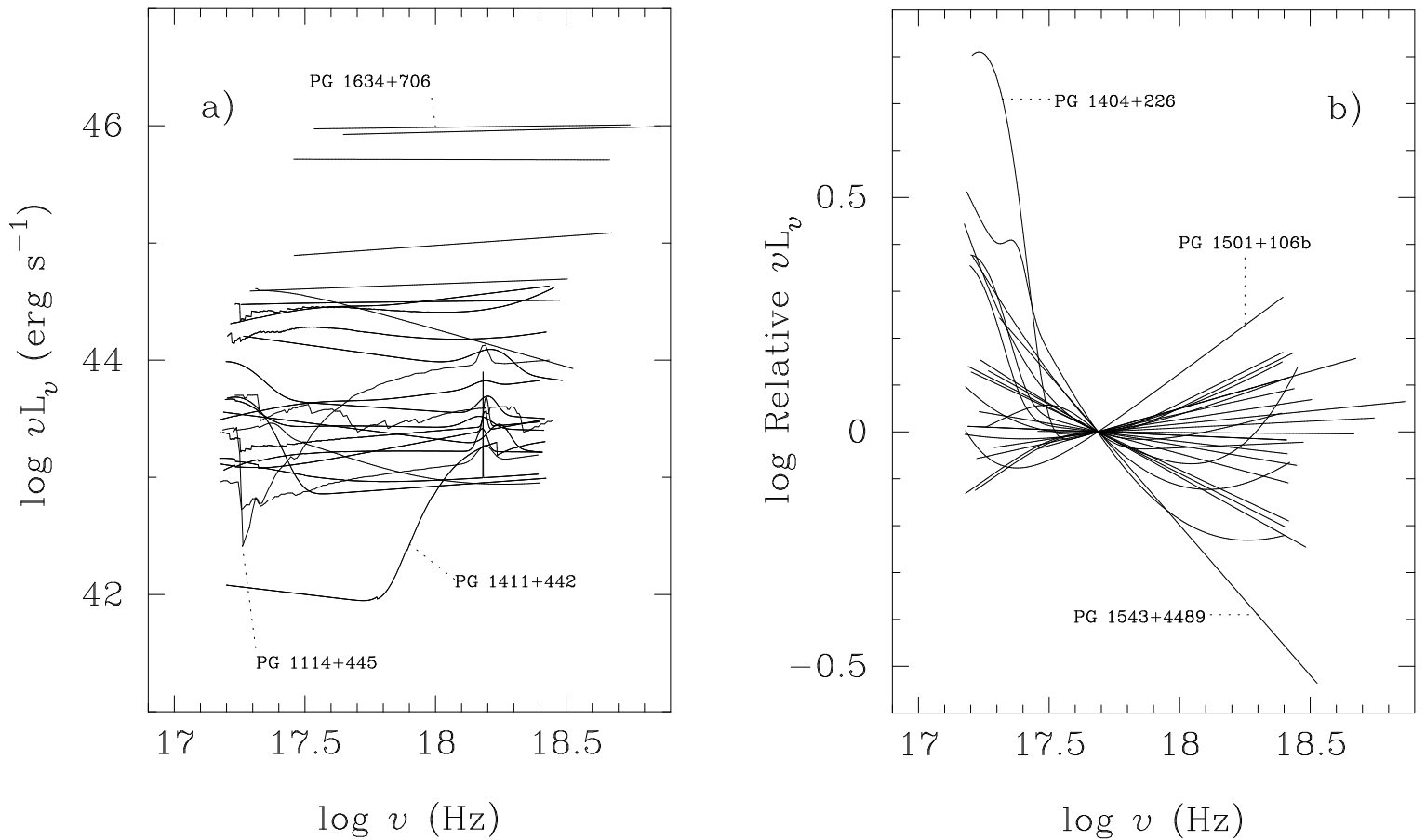


Fig. 6.— a) νL_ν versus frequency for the best-fitting models. Each curve indicates the 0.6–10 keV (observed-frame) band and has been corrected for Galactic absorption but not any absorption intrinsic to the RQQ. b) Comparison of the underlying continua when corrected for all absorption and renormalized to the luminosity at 2 keV in the quasar-frame. Any Fe K -shell emission feature is not shown for the sake of clarity. PG 1501+106b has $\Gamma \simeq 1.6$ and PG 1543+489 has $\Gamma \simeq 2.6$.

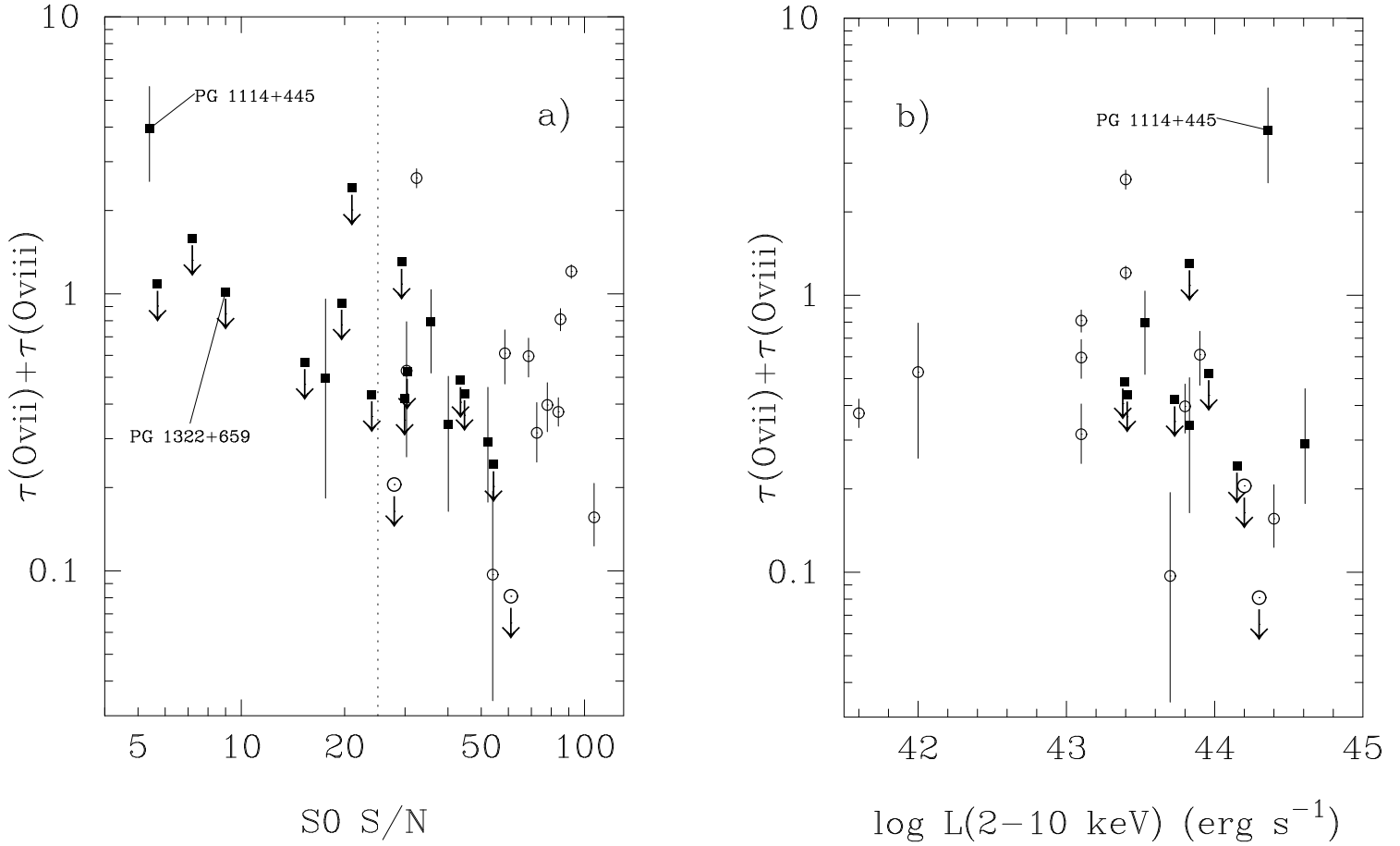


Fig. 7.— a) Sum of the optical depths of the edges due to OVII (739 eV) and OVIII (871 eV) versus signal to noise ratio (Table 10). The RQQs are shown as filled squares, and the other RQ AGN from George et al (1998a) as open circles. The dotted line indicates $S_0 S/N = 25$. The signal to noise ratio ratio for PG 1114+445 is low as a result of the deep absorption in this source. The lack of significant OVII and OVIII edges in PG 1322+659 is discussed in the text. b) Sum of the optical depths of OVII and OVIII versus luminosity in the 2–10 keV band. Only those sources with $S_0 S/N > 25$, plus PG 1114+445, are plotted.

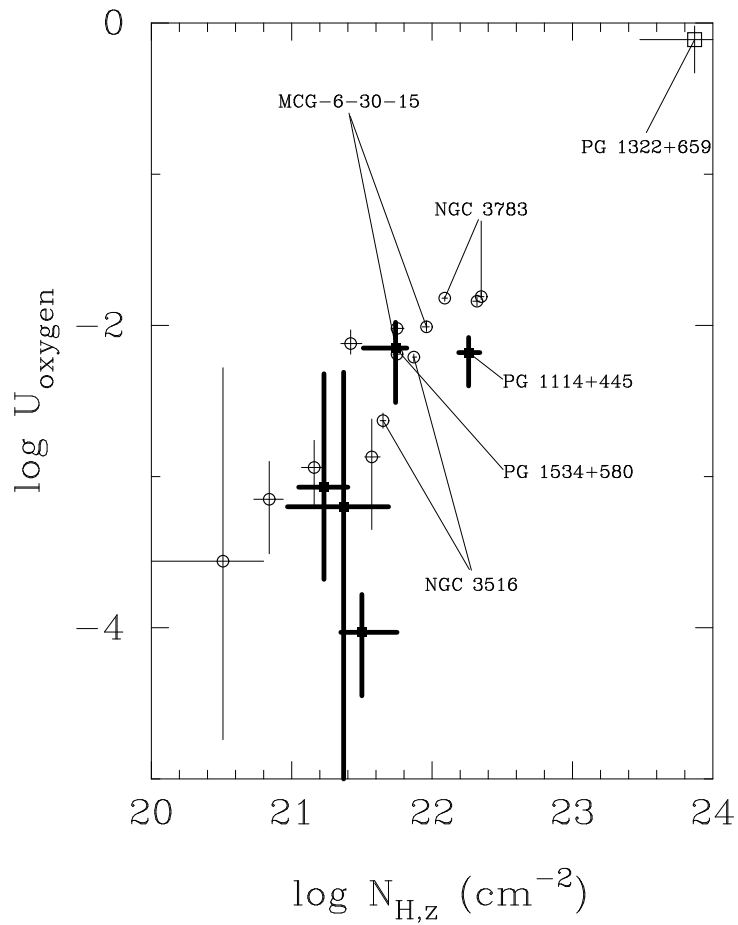


Fig. 8.— A comparison between the characteristics of the ionized absorbing material in the RQQs (squares) to those for the other RQ AGN in George et al (1998a,b,c). Besides the extreme values in the case of PG 1322+659 (which should be treated with caution – see text), we find no clear differences between the two samples.

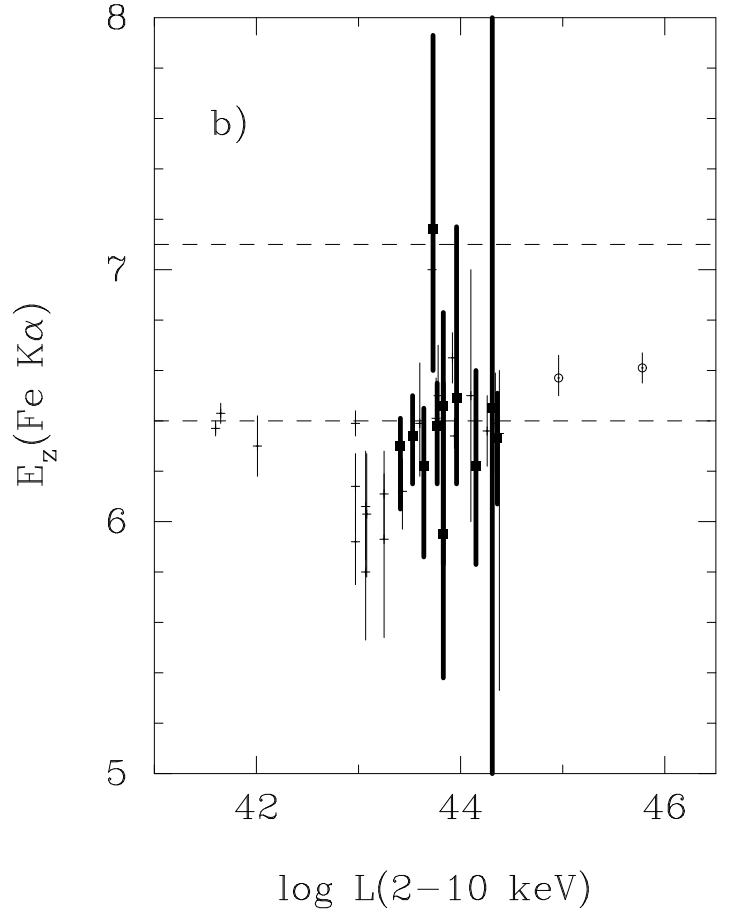
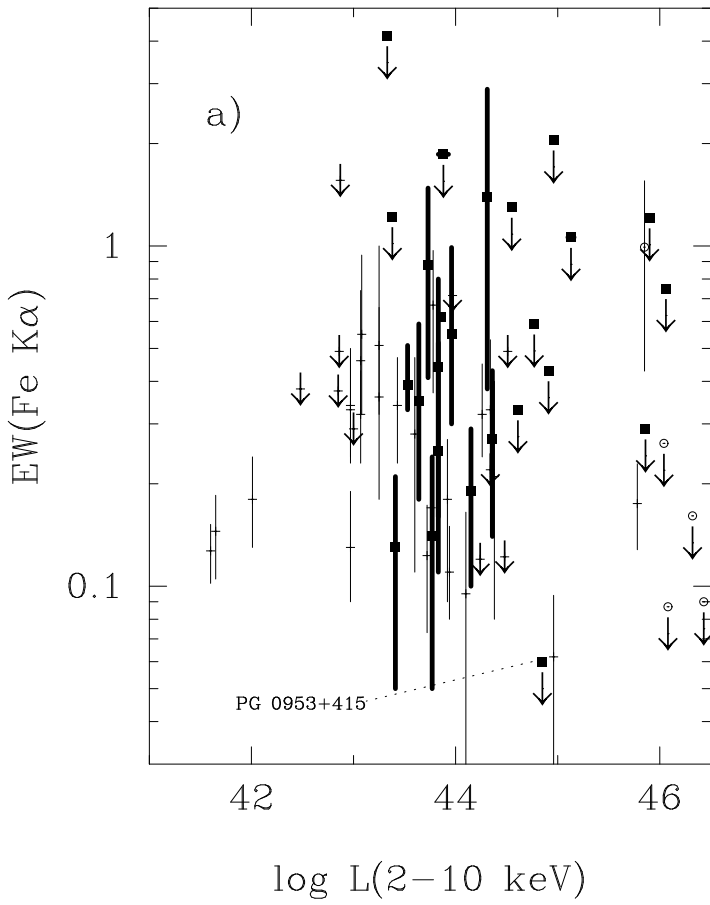


Fig. 9.— a) Luminosity in the 2–10 keV band, $L(2-10 \text{ keV})$ in units of erg s^{-1} , versus the equivalent width, $EW(\text{Fe } K\alpha)$ in units of eV, of any Fe K -shell emission. The crosses are the RQQs from Reeves et al (1997) along with Seyfert 1 Galaxies published in George et al (1998a,b,c) and Vaughan et al (1999). The circles are the high- z RQQs from Vignali, et al (1999). b) $L(2-10 \text{ keV})$ versus the energy of the line, E_z (in keV), in the quasar frame. The crosses are for the Seyfert 1 galaxies published in Nandra et al (1997b) and Vaughan et al (1999). The circles are the RQQs from Reeves et al (1997).

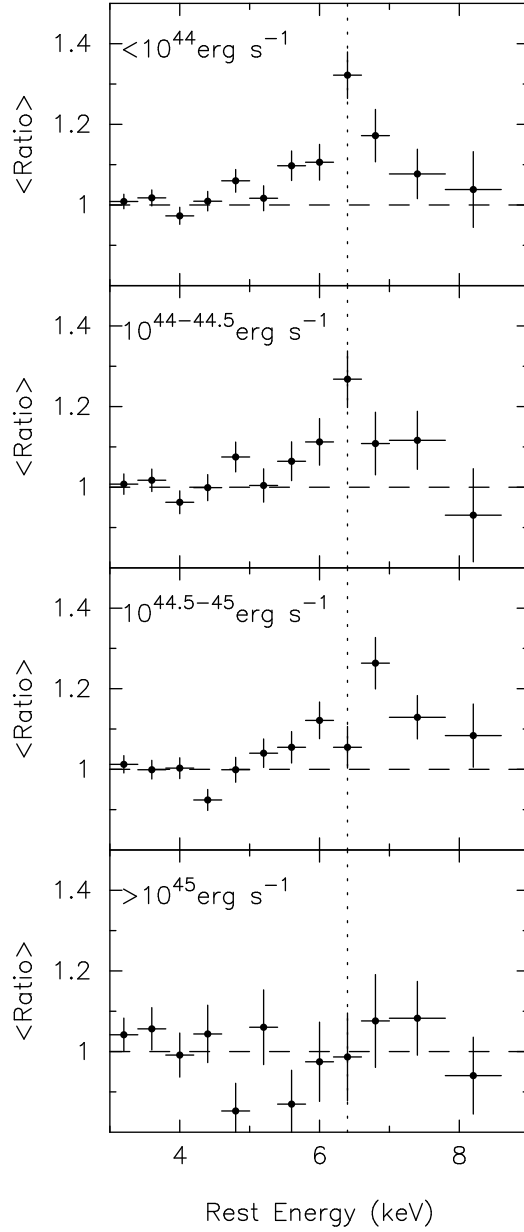


Fig. 10.— Mean SIS data/model ratios in the Fe $K\alpha$ regime as a function of 2–10 keV luminosity. Note that a different number of datasets were used in the construction of these mean profiles (from top to bottom: 12, 3, 6 & 4 datasets). The vertical dotted line at 6.4 keV indicates the energy of $K\alpha$ fluorescence from FeI–XII

Table 1. THE SAMPLE

PG Name	Alt. Name	RA	dec	z	M_V	R_L	$N_{H,0}^{gal}$	
(1)	(2)	(J2000)	(J2000)	(5)	(6)	(7)	(8)	(9)
		(3)	(4)				(10^{20} cm^{-2})	
0003+199	Mrk 335	00 06 19.3	+20 12 12	0.025	-22.13	0.27	3.70	a
0043+039	PB 6151	00 45 44.9	+04 10 57	0.384	-26.00	0.12	2.99	b
0050+124	I Zw 1	00 53 34.9	+12 41 35	0.061	-23.74	0.33	5.07	c
0804+761	...	08 10 58.5	+76 02 42	0.100	-24.43	0.60	3.26	b
0844+349	Ton 951	08 47 42.5	+34 45 05	0.064	-23.28	0.03	3.32	b
0921+525	Mrk 110	09 25 12.9	+52 17 17	0.035	-21.23	1.49	1.21	a
0953+415	...	09 56 52.5	+41 15 41	0.239	-25.67	0.44	1.12	b
1114+445	...	11 17 06.4	+44 13 33	0.144	-24.00	0.13	1.93	a
1116+215	TON 1388	11 19 08.7	+21 19 18	0.177	-25.58	0.72	1.40	b
1148+549	...	11 51 20.5	+54 37 32	0.969	-28.85	0.59	0.96	b
1211+143	...	12 14 17.6	+14 03 12	0.085	-24.60	0.13	2.76	b
1216+069	...	12 19 20.3	+06 38 40	0.334	-26.33	1.65	1.56	b
1244+026	...	12 46 35.3	+02 22 08	0.048	-21.68	0.53	1.93	c
1247+267	...	12 50 05.7	+26 31 09	2.038	-30.58	0.36	0.86	a
1322+659	...	13 23 49.6	+65 41 48	0.168	-24.16	0.12	0.19	a
1404+226	...	14 06 21.9	+22 23 47	0.098	-22.95	0.47	2.00	c
1407+265	...	14 09 23.8	+26 18 21	0.947	-28.43	3.43	1.36	b
1411+442	PB 1732	14 13 48.4	+44 00 14	0.089	-23.53	0.13	1.05	b
1416-129	...	14 19 03.8	-13 10 45	0.129	-25.05	1.15	7.20	c
1440+356	Mrk 478	14 42 07.5	+35 26 24	0.077	-23.50	0.37	0.96	a
1444+407	...	14 46 45.9	+40 35 06	0.267	-25.20	0.08‡	1.08	b
1501+106	Mrk 841	15 04 01.3	+10 26 17	0.036	-22.75	0.36	2.17	a
1534+580	Mrk 290	15 35 52.9	+57 54 09	0.030	-21.40	0.70	2.32	c
1543+489	...	15 45 30.3	+48 46 08	0.400	-25.88	0.63	1.68	b
1634+706	...	16 34 29.0	+70 31 33	1.334	-30.75	0.44	5.74	c
1700+518	...	17 01 25.0	+51 49 21	0.272	-26.31	2.40	2.48	b

Note. — Cols.(1–2): PG name and alternative name of the source in common usage. Cols.(3–4): Optical position from Green, Schmidt & Liebert (1986) transformed to J2000 coordinates. Col.(5–7): Redshift, absolute magnitude in the V-band, and radio-loudness (see §2.1). Cols.(8–9): Galactic column density from (a) Murphy et al (1996), (b) Lockman & Savage (1995), and (c) Elvis, Lockman & Wilkes (1989). The measurement errors on these values are typically $\lesssim \text{few} \times 10^{19} \text{ cm}^{-2}$.

Table 2. LOG OF THE ASCA OBSERVATIONS

Source(obs)	Start Date	Sequence	SIS C.Mode	t_{exp} (10^3 s)	t_{dur} (10^3 s)	Rate (count s $^{-1}$)	Refs
(1)	(2)	(3)	(4)	(5)	(6)	(7)	(8)
0003+199	1993 Dec 09	71010000	2	18.8	46.8	0.494 ± 0.005	a,b,c
0043+030	1996 Dec 21	74078000	2	25.8	66.5	< 0.003	d,e
0050+124	1995 Jul 15	73042000	1	27.1	92.3	0.191 ± 0.003	b,c
0804+761	1997 Nov 04	75058000	1	41.9	89.3	0.456 ± 0.003	
0844+349	1998 Apr 05	76059000	1	45.6	133.3	0.101 ± 0.002	
0921+525	1995 Apr 05	73091000	1	20.7	40.5	1.022 ± 0.007	
0953+415	1997 Nov 19	75060000	1	34.7	83.5	0.136 ± 0.002	
1114+445	1996 May 05	74072000	1	60.9	151.0	0.048 ± 0.001	f
1116+215	1995 May 19	73064000	2	17.9	40.7	0.207 ± 0.004	g
1148+549	1995 Dec 07	73037000	1	35.0	76.6	0.011 ± 0.001	
1211+143	1993 Jun 03	70025000	4	23.6	90.3	0.167 ± 0.003	b,c,h,i
1216+069	1995 Dec 25	74074000	1	21.6	42.9	0.073 ± 0.002	
1244+026	1996 Jul 01	74070000	2	36.7	103.9	0.222 ± 0.002	b,g,c
1247+267	1995 Jun 17	73048000	1	35.0	94.3	0.014 ± 0.001	
1322+659	1999 May 09	77058000	1	33.2	81.3	0.028 ± 0.001	
1404+226	1994 Jul 13	72021000	1	34.4	96.9	0.041 ± 0.001	b,c,k,l
1407+265	1993 Jul 02	70024000	1	35.3	81.3	0.059 ± 0.002	i
1411+442	1996 Dec 08	74075000	1	36.0	88.2	0.008 ± 0.001	d
1416–129	1994 Jul 29	72043000	1 & 2	0.7 & 30.1	75.4	0.344 ± 0.004	i
1440+356	1995 Jul 02	73067000	1	31.9	84.6	0.134 ± 0.002	b,c
1444+407	1997 Jan 25	75061000	1	39.9	89.0	0.037 ± 0.001	
1501+106(a)	1993 Aug 22	70009000	2	30.2	78.2	0.408 ± 0.004	a
1501+106(b)	1994 Feb 21	71040000	2	20.6	59.6	0.329 ± 0.004	a
1534+580	1994 Jun 15	72027000	2	41.0	98.3	0.271 ± 0.003	m
1543+489	1997 Jan 29	75059000	1	39.5	89.0	0.032 ± 0.001	b
1634+706	1994 May 02	71036000	1 & 2	21.9 & 20.5	47.7	0.041 ± 0.002	i
1700+518	1998 Mar 24	76041000	1	19.0	532.6	< 0.003	e

Note. — *see over*

Notes for Table 2 — Cols.(1–4): Source, Observation date (start of exposure), *ASCA* sequence number, and SIS CCD Clocking Mode in use. Col.(5–6): Total (SIS0) exposure time, t_{exp} (for each SIS clocking mode), and total duration t_{dur} between first and last events after screening. Cols.(7): Mean background-subtracted SIS0 count rate in the 0.6–10.0 keV band (uncorrected for the counts falling outside the extraction cell). In the case of PG 1416-129 & PG 1634+706 exposure-weighted mean values are quoted. Col.(8): References to other papers discussing the same dataset — (a) Nandra et al (1997a,b), George et al (1998a); (b) Vaughan et al (1999); (c) Leighly (1999); (d) Brinkmann et al (1999); (e) Gallagher et al (1999); (f) George et al (1997); (g) Nandra et al (1996); (h) Yaqoob et al (1994); (i) Reeves et al (1997); (j) Fiore et al (1998); (k) Leighly et al (1997); (l) Ulrich et al (1999); (m) Turner et al (1996).

Table 3. VARIABILITY AMPLITUDE $\sigma_{rms}^2(256 \text{ s})$

Source(obs)	SIS (0.5–10 keV)	GIS (2–10 keV)
(1)	(2)	(3)
0003+199	0.56 ± 0.19	0.72 ± 0.29
0050+124	3.76 ± 0.77	3.12 ± 0.68
0804+761	0.16 ± 0.07	< 0.26
0844+349	0.88 ± 0.31	0.91 ± 0.42
0921+525	< 0.14	< 0.19
0953+415	< 0.52	< 0.40
1116+215	< 0.43	< 0.57
1211+143	...	< 1.12
1244+026	3.83 ± 0.64	4.26 ± 0.78
1322+659	8.30 ± 0.29	...
1416–129	< 0.15	< 0.46
1440+356	1.87 ± 0.49	1.91 ± 0.54
1501+106(a)	0.74 ± 0.20	0.58 ± 0.18
1501+106(b)	0.46 ± 0.22	< 0.30
1534+580	4.02 ± 0.51	3.50 ± 0.48

Note. — Normalized excess variance, $\sigma_{rms}^2(256 \text{ s})$ in units of 10^{-2} . Upper limits are at 90% confidence. Lack of an entry indicates the criteria described in §3 were not fulfilled.

Table 4. MODEL A APPLIED TO THE 2-10 keV (QUASAR-FRAME) CONTINUUM
(see §4.1.1)

Source(obs)	N_{pts}	Γ_{2-10}	χ^2_ν	$P(\chi^2)$
(1)	(2)	(3)	(4)	(5)
0003+199	331	$1.94^{+0.03}_{-0.04}$	0.98	0.41
0050+124	202	$2.25^{+0.06}_{-0.07}$	1.02	0.60
0804+761	529	$2.18^{+0.02}_{-0.03}$	1.02	0.65
0844+349	236	$1.97^{+0.06}_{-0.06}$	0.93	0.23
0921+525	618	$1.78^{+0.03}_{-0.04}$	1.05	0.79
0953+415	230	$2.03^{+0.06}_{-0.05}$	0.98	0.44
1114+445	289	$1.51^{+0.04}_{-0.05}$	1.08	0.82
1116+215	188	$2.06^{+0.06}_{-0.06}$	1.11	0.86
1148+549	73	$1.83^{+0.16}_{-0.15}$	0.96	0.43
1211+143	223	$2.00^{+0.05}_{-0.06}$	0.82	0.02
1216+069	120	$1.76^{+0.09}_{-0.08}$	0.83	0.10
1244+026	225	$2.46^{+0.06}_{-0.06}$	0.92	0.20
1247+267	68	$2.07^{+0.15}_{-0.15}$	0.82	0.16
1322+659	90	$1.63^{+0.14}_{-0.14}$	0.91	0.28
1404+226	64	$1.75^{+0.23}_{-0.22}$	1.13	0.76
1407+265	196	$2.05^{+0.05}_{-0.05}$	0.86	0.08
1411+442	58	$-0.42^{+0.24}_{-0.26}$	1.49	0.99
1416–129	531	$1.79^{+0.03}_{-0.02}$	1.02	0.65
1440+356	193	$2.06^{+0.06}_{-0.07}$	0.92	0.21
1444+407	111	$2.21^{+0.13}_{-0.13}$	1.07	0.71
1501+106(a)	449	$1.77^{+0.03}_{-0.03}$	1.03	0.66
1501+106(b)	255	$1.60^{+0.04}_{-0.04}$	0.97	0.36
1534+580	492	$1.68^{+0.02}_{-0.03}$	0.94	0.17
1543+489	93	$2.80^{+0.18}_{-0.16}$	0.78	0.06
1634+706	175	$2.03^{+0.06}_{-0.06}$	1.18	0.95

Note. — *see over*

Notes to Table 4 — Results of fitting a single power-law with galactic absorption to the 2–10 keV band, excluding the 5–7 keV band. Col.(1–2): Dataset and number of data points used in the spectral analysis (sum of all instruments). Col.(3): Best-fitting value of the photon index of the underlying power law with errors quoted at 68% confidence for 1 interesting parameter. Cols.(4–5): Reduced- χ^2 statistic (χ^2_ν) and probability ($P(\chi^2)$) that the χ^2 -statistic will be less than the observed value for the number of *dof*. The model is considered an acceptable representation of the data ($P(\chi^2) \leq 0.95$) in all cases except PG 1411+442.

Table 5. SUMMARY OF THE PREFERRED MODEL FOR THE FULL *ASCA* CONTINUUM

Source(obs)	Preferred Model	F_{2-10}	$F_{\nu}(2 \text{ keV})$	$\log L(2-10 \text{ keV})$	Notes
(1)	(2)	(3)	(4)	(5)	(6)
0003+199	D	9.44 ± 0.10	3.00 ± 0.03	43.41 ± 0.02	Var., SXS, Fe
0043+039	‡	< 0.07	< 0.03	< 43.78	
0050+124	A	3.22 ± 0.04	1.35 ± 0.02	43.73 ± 0.01	Var., Fe (?)
0804+761	E	8.79 ± 0.07	3.84 ± 0.04	44.61 ± 0.01	Abs
0844+349	B	2.36 ± 0.02	0.72 ± 0.01	43.64 ± 0.01	Var., Abs, Fe
0921+525	F	26.85 ± 0.19	7.21 ± 0.05	44.15 ± 0.01	Fe
0953+415	F	2.59 ± 0.04	1.08 ± 0.02	44.85 ± 0.01	
1114+445	C	2.13 ± 0.05	0.72 ± 0.02	44.36 ± 0.01	Abs, Fe
1116+215	E	3.94 ± 0.07	1.68 ± 0.03	44.77 ± 0.01	Var. ? Abs ?
1148+549	A	0.27 ± 0.02	0.13 ± 0.01	45.13 ± 0.03	SXS (?) †
1211+143	F	2.78 ± 0.04	1.08 ± 0.02	43.96 ± 0.01	Var. ? SXS, Fe
1216+069	A	1.72 ± 0.05	0.65 ± 0.02	44.96 ± 0.02	
1244+026	D+Ga	2.32 ± 0.03	1.22 ± 0.01	43.38 ± 0.01	Var., 1 keV line †
1247+267	A	0.29 ± 0.02	0.25 ± 0.02	45.90 ± 0.03	
1322+659	C	0.54 ± 0.02	0.14 ± 0.01	43.86 ± 0.02	Abs
1404+226	F	0.51 ± 0.02	0.15 ± 0.01	43.33 ± 0.02	SXS, Var.
1407+265	A	1.38 ± 0.04	0.84 ± 0.02	45.86 ± 0.01	
1411+442	B _{pc}	0.76 ± 0.09	0.90 ± 0.11	43.88 ± 0.05	Abs †
1416–129	F	11.08 ± 0.24	0.33 ± 0.01	44.91 ± 0.01	
1440+356	F	2.54 ± 0.04	0.91 ± 0.02	43.83 ± 0.01	Var., SXS, Fe
1444+407	A	0.55 ± 0.02	0.29 ± 0.01	44.31 ± 0.01	Fe (?)
1501+106(a)	E	11.90 ± 0.12	3.46 ± 0.03	43.83 ± 0.01	Var., SXS, Abs, Fe
1501+106(b)	D	10.41 ± 0.14	2.36 ± 0.03	43.77 ± 0.01	SXS, Fe
1534+580	E	8.49 ± 0.08	2.40 ± 0.02	43.53 ± 0.01	Var., Abs, Fe
1543+489	B	0.36 ± 0.01	0.31 ± 0.01	44.55 ± 0.02	
1634+706	A	1.04 ± 0.04	0.72 ± 0.03	46.06 ± 0.01	†
1700+518	‡	< 0.08	< 0.03	< 43.51	

Note. — *see over*

Notes to Table 5 — Cols.(1–2): Dataset, and preferred spectral model for the continuum (see §4.1). For the two sources not detected (§), upper limits are calculated assuming Model A with $\Gamma = 2.0$. Col.(3): Flux in the *observed* 2–10 keV band in units of 10^{-12} erg cm $^{-2}$ s $^{-1}$. Col.(4): Specific intensity, corrected for absorption, at 2 keV in the *quasar-frame* in units of 10^{-12} erg cm $^{-2}$ s $^{-1}$ keV $^{-1}$ ($\simeq 0.41 \times 10^{-6}$ Jy). Col.(5): Luminosity, corrected for absorption, in the 2–10 keV band (*quasar-frame*) in units of erg s $^{-1}$ assuming $H_0 = 50$ km s $^{-1}$ Mpc $^{-1}$ and $q_0 = 0.5$. Col.(6): Var. – Variable source (Table 3); SXS – soft X-ray component; Abs – intrinsic absorption, Fe – Fe *K*-shell emission (Table 9), † – see text.

Table 6. BEST-FITTING PARAMETERS OF RQQs FOR WHICH MODELS A, B or C IS PREFERRED

Source(obs)	$N_{H,z}$	$\log U_{oxygen}$	Γ	N_{pts}	χ^2_ν	$P(\chi^2)$
(1)	(2)	(3)	(4)	(5)	(6)	(7)
0050+124	$2.28^{+0.02}_{-0.02}$	420	0.95	0.26
0844+349	$0.68^{+0.28}_{-0.28}$...	$2.02^{+0.07}_{-0.06}$	457	1.07	0.87
1114+445	$18.20^{+4.45}_{-3.54}$	$-2.184^{+0.126}_{-0.275}$	$1.87^{+0.16}_{-0.11}$	439	1.02	0.61
1148+549	$1.84^{+0.11}_{-0.10}$	114	0.81	0.07
1216+069	$1.92^{+0.04}_{-0.05}$	219	0.86	0.06
1247+267	$1.95^{+0.08}_{-0.09}$	114	0.86	0.14
1322+659	$758^{+241}_{-522} (p)$	$-0.105^{+0.089}_{-0.273}$	$2.10^{+0.12}_{-0.11}$	214	0.90	0.16
1407+265	$2.01^{+0.03}_{-0.04}$	272	0.89	0.11
1411+442 ‡	244^{+113}_{-83}	...	$2.26^{+0.78}_{-0.74}$	103	1.16	0.87
1444+407	$2.31^{+0.05}_{-0.05}$	229	1.03	0.65
1543+489	$0.69^{+1.14}_{-0.69} (p)$...	$2.64^{+0.19}_{-0.16}$	203	0.93	0.25
1634+706	$1.97^{+0.04}_{-0.04}$	240	1.29	0.98 †

Note. — Fits undertaken in the *observed* 0.6–10.0 keV band, but excluding the 5–7 keV band in the *quasar-frame*. All models include Galactic absorption of column density $N_{H,0}^{gal}$ as given in Table 1. Errors are at 68% confidence for the relevant number of interesting parameters. ‡ The model for PG 1411+442 includes a fraction $D_f = 0.02^{+0.06}_{-0.01}$ of the continuum which does not suffer attenuation. Col.(1): Dataset. Col.(2): Column density of absorbing material intrinsic to the quasar in units of 10^{21} cm^{-2} (Models B & C only). Col.(3): Ionization parameter of the absorbing material as defined in §4.1 (Model C only). Col.(4): Photon index of the power law continuum. Cols.(5–7): Number of data points used in the spectral analysis (N_{pts}), reduced- χ^2 statistic (χ^2_ν) and probability ($P(\chi^2)$) that the χ^2 -statistic will be less than the observed value for the number of *dof*. † see text.

Table 7. BEST-FITTING PARAMETERS OF RQQs FOR WHICH MODELS D or E IS PREFERRED

Source(obs)	$N_{H,z}$	$\log U_{oxygen}$	Γ_s	$\log R_s/h$	Γ_h	N_{pts}	χ^2_ν	$P(\chi^2)$
(1)	(2)	(3)	(4)	(5)	(6)	(7)	(8)	(9)
0003+199	$0.90^{+1.31}_{-0.90}$ (p)	...	$4.18^{+0.82}_{-1.11}$ (p)	$-0.01^{+0.44}_{-0.41}$	$1.84^{+0.15}_{-0.16}$	627	0.97	0.28
0804+761	$3.16^{+3.74}_{-1.94}$	$-4.04^{+0.42}_{-1.40}$	$3.00^{+1.71}_{-0.58}$	$+0.90^{+1.62}_{-0.61}$	$1.43^{+0.77}_{-0.72}$	803	1.04	0.78
1116+215	$2.34^{+4.58}_{-1.88}$	$-3.20^{+1.24}_{-2.11}$ (p)	$2.36^{+1.57}_{-0.26}$	$+2.30^{+0.62}_{-1.42}$	$0.00^{+0.00}_{-1.25}$ (p)	354	1.05	0.75
1244+026 ‡	$1.01^{+2.19}_{-0.99}$...	$3.24^{+1.76}_{-0.61}$ (p)	$+0.95^{+2.10}_{-5.00}$ (p)	$1.60^{+0.89}_{-1.60}$ (p)	504	1.08	0.89
1501+106(a)	$1.70^{+3.87}_{-0.93}$	$-3.07^{+1.07}_{-2.24}$	$3.61^{+1.49}_{-2.11}$ (p)	$-0.51^{+1.41}_{-1.07}$	$1.80^{+0.10}_{-0.14}$	742	1.02	0.78
1501+106(b)	$0.30^{+0.16}_{-0.30}$ (p)	...	$5.00^{+0.00}_{-1.58}$ (p)	$-0.88^{+0.55}_{-0.24}$	$1.59^{+0.06}_{-0.05}$	421	0.93	0.16
1534+580	$5.50^{+1.98}_{-2.64}$	$-2.15^{+0.26}_{-1.78}$	$2.39^{+2.61}_{-0.89}$ (p)	$+0.10^{+4.90}_{-2.66}$ (p)	$1.57^{+0.93}_{-1.26}$ (p)	780	1.07	0.90

Note. — Symbols and units as for Table 6, except Cols.(4–6) contain the best-fitting values for the photon indices for the ‘soft’ and ‘hard’ power laws (Γ_s & Γ_h) and R_s/h , the ratio of the normalizations of the soft to hard power laws at 1 keV (in the quasar-frame). (p) indicates the parameter ‘pegged’ at the specified value. ‡ The model for PG 1244+026 includes a Gaussian emission line with $E_z = 0.96^{+0.07}_{-0.31}$ keV, $\sigma_z = 0.09^{+0.16}_{-0.09}$ keV, and $L_{line} \simeq 3 \times 10^{42}$ erg s⁻¹ (see text).

Table 8. BEST-FITTING PARAMETERS OF RQQs FOR WHICH MODEL F IS PREFERRED

Source(obs)	$N_{H,z}$	Γ	E_z	σ_z	$\log L_{line}$	N_{pts}	χ^2_ν	$P(\chi^2)$
(1)	(2)	(3)	(4)	(5)	(6)	(7)	(8)	(9)
0921+525	$0.10^{+0.30}_{-0.10}$ (<i>p</i>)	$1.73^{+0.08}_{-0.08}$	$0.36^{+0.87}_{-0.06}$ (<i>p</i>)	$0.76^{+0.13}_{-0.43}$	$43.04^{+0.16}_{-0.94}$	914	1.04	0.80
0953+415	$0.01^{+1.09}_{-0.01}$ (<i>p</i>)	$1.98^{+0.17}_{-0.15}$	$0.71^{+0.80}_{-0.28}$	$0.60^{+0.21}_{-0.22}$	$44.10^{+0.37}_{-0.54}$	403	0.97	0.36
1211+143 ‡	$0.00^{+0.28}_{-0.00}$ (<i>p</i>)	$2.16^{+0.04}_{-0.08}$	$0.38^{+0.13}_{-0.01}$	$0.24^{+0.01}_{-0.05}$	$43.99^{+0.13}_{-0.25}$	480	0.93	0.15
1404+026 ‡	$0.00^{+0.49}_{-0.00}$ (<i>p</i>)	$1.82^{+0.29}_{-0.26}$	$0.39^{+0.10}_{-0.01}$	$0.28^{+0.02}_{-0.04}$	$43.73^{+0.13}_{-0.17}$	166	1.01	0.53
1416–129	$0.12^{+0.58}_{-0.12}$ (<i>p</i>)	$1.73^{+0.11}_{-0.09}$	$0.40^{+0.95}_{-0.10}$ (<i>p</i>)	$0.81^{+0.17}_{-0.54}$	$43.83^{+0.19}_{-1.20}$	867	0.98	0.37
1440+356 ‡	$0.54^{+1.53}_{-0.54}$ (<i>p</i>)	$2.06^{+0.17}_{-0.11}$	$0.43^{+0.71}_{-0.06}$	$0.22^{+0.05}_{-0.13}$	$43.67^{+0.33}_{-1.03}$	384	0.92	0.13

Note. — Symbols and units as for Table 6, except cols.(4–6) which contain the energy, width and equivalent width of the Gaussian component (all in keV). ‡ In the case of PG 1211+143, PG 1404+026 and PG1440+356 the Gaussian represents a *parameterization* of a 'soft-excess'. The Gaussian parameterizes only subtle curvature of the underlying continuum in the other cases.

Table 9. FE EMISSION LINE PARAMETERS

Source(obs)	ΔN_{pts}	$\frac{\Delta\chi^2}{\Delta N_{pts}}$	F	E_z (keV)	σ_z (keV)	$EW(\text{Fe-K})$ (keV)	$\log L(\text{Fe-K})$ (erg s ⁻¹)
(1)	(2)	(3)	(4)	(5)	(6)	(7)	(8)
0003+199	73	0.93	3.90	6.30 ^{+0.11} _{-0.25}	< 1.20	0.13 ^{+0.08} _{-0.08}	41.52 ^{+0.21} _{-0.42}
0050+124 ‡	38	1.47	4.86	7.16 ^{+0.77} _{-0.56}	0.63 ^{+0.53} _{-0.33}	0.88 ^{+0.60} _{-0.47}	42.57 ^{+0.23} _{-0.33}
0804+761	137	0.93	1.32	< 0.33	< 43.14
0844+349	58	1.30	15.12	6.22 ^{+0.23} _{-0.36}	< 1.96	0.35 ^{+0.24} _{-0.17}	42.21 ^{+0.23} _{-0.29}
0921+525	172	0.97	7.33	6.22 ^{+0.38} _{-0.39}	0.76 ^{+0.30} _{-0.55}	0.19 ^{+0.10} _{-0.09}	42.48 ^{+0.19} _{-0.30}
0953+415	54	0.91	1.40	< 0.06	< 42.69
1114+445	86	1.02	5.61	6.33 ^{+0.18} _{-0.26}	< 0.85	0.27 ^{+0.16} _{-0.13}	42.80 ^{+0.20} _{-0.29}
1116+215	43	1.02	2.30	< 0.59	< 43.58
1148+549	21	0.68	0.87	< 1.06	< 44.32
1211+143	50	1.66	7.74	6.49 ^{+0.68} _{-0.34}	0.52 ^{+1.16} _{-0.28}	0.55 ^{+0.44} _{-0.25}	42.69 ^{+0.25} _{-0.25}
1216+069	31	1.38	1.48	< 2.05	< 44.26
1244+026	45	1.00	2.88	< 1.22	< 42.41
1247+267	31	0.71	0.40	< 1.21	< 45.18
1322+659	22	1.36	0.01	< 0.62	< 42.91
1404+226	21	0.90	1.79	< 4.15	< 42.95
1407+265	44	1.00	1.49	< 0.29	< 44.50
1411+442	26	1.04	1.23	< 1.86	< 42.80
1416-129	145	1.17	1.67	< 0.43	< 43.60
1440+356	43	1.53	4.25	5.95 ^{+0.88} _{-0.57}	...	0.44 ^{+0.36} _{-0.33}	42.50 ^{+0.26} _{-0.61}
1444+407 ‡	28	1.32	3.27	6.45 ^{+1.55} _{-1.47} (<i>p</i>)	...	1.39 ^{+1.50} _{-1.01}	43.44 ^{+0.32} _{-0.57}
1501+106(a)	114	1.18	11.00	6.46 ^{+0.09} _{-0.63}	0.13 ^{+0.70} _{-0.09}	0.25 ^{+0.27} _{-0.09}	42.24 ^{+0.32} _{-0.19}
1501+106(b)	69	1.04	3.70	6.38 ^{+0.17} _{-0.23}	< 1.03	0.14 ^{+0.10} _{-0.09}	41.96 ^{+0.23} _{-0.44}
1534+580	134	1.12	17.16	6.34 ^{+0.16} _{-0.19}	0.41 ^{+0.21} _{-0.15}	0.38 ^{+0.12} _{-0.06}	42.14 ^{+0.12} _{-0.07}
1543+489	25	1.08	1.83	< 1.30	< 43.74
1634+706	46	0.63	1.16	< 0.75	< 45.25

Note. — Col.(1): Dataset. Col.(2,3): Number of additional spectral bins (ΔN_{pts}) and fractional increase in the χ^2 -statistic per additional bin ($\Delta\chi^2/\Delta N_{pts}$) when the preferred model from §4.1.2 is applied to the data in the 5–7 keV band (quasar-frame). Col.(4): F -statistic when a Gaussian emission component is added to the spectral analysis. Cols.(5–8): Energy (E_z), width (σ_z), equivalent width (EW), and luminosity of the Gaussian component. ‡ Line parameters considered dubious (see text).

Table 10. CONSTRAINTS ON OVII AND OVIII EDGES

Source(obs)	S0 S/N	$\tau(\text{OVII})$	$\tau(\text{OVIII})$
(1)	(2)	(3)	(4)
0003+199	45	$0.16^{+0.12}_{-0.12}$	< 0.07
0050+124	30	< 0.29	< 0.06
0804+761	52	$0.29^{+0.13}_{-0.11}$	< 0.03
0844+349	24	< 0.32	< 0.11
0921+525	54	< 0.09	< 0.10
0953+415	20	< 0.41	< 0.29
1114+445	5	$2.56^{+1.18}_{-0.65}$	$1.39^{+0.48}_{-0.76}$
1116+215	18	$0.44^{+0.27}_{-0.26}$	< 0.26
1211+143	30	< 0.10	< 0.15
1216+069	6	< 0.27	< 0.14
1244+026	44	< 0.24	< 0.09
1322+659	9	< 0.53	< 0.24
1404+226	21	< 0.93	$0.40^{+0.60}_{-0.30}$
1411+442	3	< 1.14	< 1.65
1416–129	15	< 0.32	< 0.11
1440+356	29	< 0.82	< 0.25
1444+407	10	< 0.37	< 0.19
1501+106(a)	40	$0.28^{+0.11}_{-0.12}$	< 0.14
1501+106(b)	28	< 0.28	< 0.14
1534+580	36	$0.48^{+0.16}_{-0.15}$	$0.31^{+0.09}_{-0.13}$
1543+489	7	< 0.63	< 0.47

Note. — Col.(1): Dataset (sources with $z > 0.45$ are excluded). Col.(2): The signal-to-noise ratio of the SIS0 data between 0.6 keV (observed frame) and 1 keV (quasar frame). Cols.(3,4): Constraints on the optical depth of the two edges.

Table 11. SERENDIPTOUS SOURCES WITHIN THE FIELDS OF VIEW

PG Field	RA	dec	GIS2 Rate	Possible Identification		
	J2000	J2000	(10^{-2} ct s $^{-1}$)	Name	Class	Refs
(1)	(2)	(3)	(4)	(5)	(6)	(7)
0804+761	08 12 48.8	+76 06 12	1.35 ± 0.07	1RXS J081241.7+760615
1216+069	12 20 16.3	+06 41 20	1.42 ± 0.09	1RXS J122019.0+064126
1216+069	12 19 28.1	+06 42 59	0.99 ± 0.08	2E 1216.9+0700	AGN	St91
1247+267	12 49 46.7	+26 29 07	0.34 ± 0.04	1RXP J124946+262
1404+226	14 05 29.0	+22 23 50	0.71 ± 0.06	1RXP J140528+2223.4
1440+356	14 41 07.4	+35 20 29	0.47 ± 0.05	1WGA J1441.1+3519
1501+106	15 03 36.9	+10 16 44	0.69 ± 0.08	1RXP J150340+1016.3
1501+106	15 04 25.6	+10 29 33	0.16 ± 0.04	PKS 1502+106	AGN	Ge94

Note. — Col.(1–3): Target field and position of serendipitous source as determined from the GIS data after correcting for any offset (typically $\lesssim 1$ arcmin) between the target source and catalogued position listed in Table 1. Cols.(4): GIS2 count rates in the 1–10 keV (observer’s frame) band. The extraction cells varied, but were typically circular of radius 1.5–2.5 arcmin. Cols.(5–6): Tentative identification from a cross-correlation with previously detected X-ray sources and (if known) the class of the object. Col.(8): References discussing X-ray observations of the serendipitous source: St91 - Stocke et al (1991), Ge94 - George et al (1994). Two additional sources were detected: tentatively identified as the cluster of galaxies ACO 1885 (in the PG 1411+442 field) and the AGN 1E 0803.3+7557 (in the PG 0804+761 field). However both objects lie close to the edge of the GIS field-of-view and an accurate position or count rate are not possible using these *ASCA* data.